Stem Cell Reports
Article
ISSCR
OPEN ACCESS

Human iPSC model reveals a central role for NOX4 and oxidative stress in Duchenne cardiomyopathy

Robin Duelen,[1] Domiziana Costamagna,[1,2] Guillaume Gilbert,[3] Liesbeth De Waele,[4] Nathalie Goemans,[4] Kaat Desloovere,[2] Catherine M. Verfaillie,[5] Karin R. Sipido,[3] Gunnar M. Buyse,[4] and Maurilio Sampaolesi[1,6,*]
[1]Translational Cardiomyology Lab, Stem Cell and Developmental Biology, Department of Development and Regeneration, KU Leuven, Herestraat 49 – O&N4 – bus 804, 3000 Leuven, Belgium
[2]Research Group for Neurorehabilitation, Department of Rehabilitation Sciences, KU Leuven, 3000 Leuven, Belgium
[3]Experimental Cardiology, Department of Cardiovascular Sciences, KU Leuven, 3000 Leuven, Belgium
[4]Pediatric Neurology, University Hospitals Leuven, Department of Development and Regeneration, KU Leuven, 3000 Leuven, Belgium
[5]Stem Cell Institute Leuven, Stem Cell and Developmental Biology, Department of Development and Regeneration, KU Leuven, 3000 Leuven, Belgium
[6]Histology and Medical Embryology Unit, Department of Anatomy, Histology, Forensic Medicine and Orthopedics, Sapienza University of Rome, 00185 Rome, Italy
*Correspondence: maurilio.sampaolesi@kuleuven.be
https://doi.org/10.1016/j.stemcr.2021.12.019

SUMMARY

Duchenne muscular dystrophy (DMD) is a progressive muscle disorder caused by mutations in the *Dystrophin* gene. Cardiomyopathy is a major cause of early death. We used DMD-patient-specific human induced pluripotent stem cells (hiPSCs) to model cardiomyopathic features and unravel novel pathologic insights. Cardiomyocytes (CMs) differentiated from DMD hiPSCs showed enhanced premature cell death due to significantly elevated intracellular reactive oxygen species (ROS) resulting from depolarized mitochondria and increased NADPH oxidase 4 (NOX4). CRISPR-Cas9 correction of *Dystrophin* restored normal ROS levels. ROS reduction by N-acetyl-L-cysteine (NAC), ataluren (PTC124), and idebenone improved hiPSC-CM survival. We show that oxidative stress in DMD hiPSC-CMs was counteracted by stimulating adenosine triphosphate (ATP) production. ATP can bind to NOX4 and partially inhibit the ROS production. Considering the complexity and the early cellular stress responses in DMD cardiomyopathy, we propose targeting ROS production and preventing detrimental effects of NOX4 on DMD CMs as promising therapeutic strategy.

INTRODUCTION

The shortage of human cardiac cell sources has challenged cardiovascular disease modeling and drug development. The generation of functional cardiomyocytes (CMs) differentiated from human induced pluripotent stem cells (hiPSCs) overcomes current limitations and offers an extraordinary platform to develop hiPSC-based models to study the genetic disease phenotype of cardiomyopathic pathologies *in vitro* (Mummery et al., 2012; Takahashi and Yamanaka, 2006).

Mutations in the *Dystrophin* gene cause the X-linked disorder Duchenne muscular dystrophy (DMD), the most common and severe phenotype among the muscular dystrophies (Mercuri et al., 2019). Most DMD patients develop adverse myocardial remodeling and chronic cardiomyopathy, a major cause of morbidity and early mortality (Emery, 2002). With the current standards of care, the median life expectancy at birth in individuals with DMD has improved during the last decades and ranges between 21.0 and 39.6 years (Landfeldt et al., 2020).

The Dystrophin protein has a crucial role during muscle contraction and stretch. Loss of function or absence lead to myocyte sarcolemma instability during contraction-relaxation cycles, making myocytes more susceptible to stretch-induced damage and necrosis (Davies and Nowak, 2006). The signaling-mediated roles of Dystrophin and the associated dystrophin glycoprotein complex are not yet fully understood (Allen et al., 2016). The pathophysiological role of Dystrophin in the heart is poorly defined, and multiple pathways are involved including dysregulation of calcium (Ca^{2+}) homeostasis, oxidative stress, inflammation, and functional ischemia.

Oxidative stress is involved in the pathogenesis of heart failure. However, clinical trials using antioxidants have shown limited success (Sesso et al., 2008). Nicotinamide adenine dinucleotide phosphate (NADPH) oxidase (NOX) family enzymes generate reactive oxygen species (ROS) in a highly regulated manner, modulating several physiological aspects such as host defense, posttranslational processing of proteins, cellular signaling, regulation of gene expression, and cell differentiation (Vermot et al., 2021). However, NOX family enzymes also contribute to a wide range of pathological processes, including, in particular, cardiovascular diseases. The NOX4 isoform is predominantly expressed in CMs, although the precise location remains controversial. It is constitutively active at low levels, inducing cardioprotective effects under chronic stress. The exact role of NOX4 in CMs is still not clear, even though high levels of NOX4 could have severe detrimental effects (Ago et al., 2010; Varga et al., 2017; Zhang et al., 2013) including excessive ROS production (Spurney et al.,

2008). Thus, targeting NOX isoforms may be a useful therapeutic strategy.

Several innovative therapeutic approaches focus on targeting the primary defect such as restoring the function or expression of Dystrophin through exon skipping (Wu et al., 2008), ribosomal readthrough technology (Welch et al., 2007), or gene (Moretti et al., 2020) and cell therapy (Bajek et al., 2015). Recent technological breakthroughs in genome editing successfully enabled the correction of the genetic mutation (Calos, 2016). In addition, compounds targeting downstream pathophysiology are under investigation in clinical trials (Verhaart and Aartsma-Rus, 2019). 2,3-dimethoxy-5-methyl-6-(10-hydroxy)decyl-1,4-benzoquinone (idebenone), a synthetic analogue of coenzyme Q_{10}, has a dual mode of action. First, it detoxifies ROS by donating electrons to produce non-toxic reaction products. Second, it donates electrons directly to complex III of the mitochondrial electron transport chain (ETC), which restores electron flow, proton pumping activity of complexes III and IV, and adenosine triphosphate (ATP) production by complex V. Phase 2/3 randomized, placebo-controlled trials have demonstrated a beneficial role of idebenone in DMD patients (Buyse et al., 2015).

In this study, we used DMD-patient-specific hiPSC-derived CMs (hiPSC-CMs) to model cardiomyopathic features to explore pathological mechanisms. We observed mitochondrial dysfunction and high intracellular ROS concentrations in DMD hiPSC-CMs due to significantly increased NOX4. These features were not present in CRISPR-Cas9 genetically corrected DMD isogenic hiPSC-CMs. Additionally, by administration of the ROS scavenger N-acetyl-L-cysteine (NAC), the readthrough chemical drug ataluren (PTC124), or the synthetic benzoquinone idebenone, we observed beneficial outcomes regarding the survival and function of differentiated DMD hiPSC-CMs.

In conclusion, using DMD-patient-derived hiPSCs, we established an *in vitro* model to recapitulate DMD heart disease phenotypes and to study novel disease mechanisms that might become interesting therapeutic targets for cardiomyopathy in DMD patients.

RESULTS

Generation of integration-free DMD hiPSCs

To obtain an unlimited cell source of CMs, recapitulating aspects of a single-gene disease phenotype, hiPSC lines were generated from human dermal fibroblasts (hFs) and human peripheral blood mononuclear cells (hPBMCs) obtained from DMD patients with known *Dystrophin* mutations (Table S1). Somatic cells were reprogrammed toward a pluripotent state using integration-free Sendai virus (SeV) vectors (Figures S1A–S1C), which expressed the OSKM (OCT3/4, SOX2, KLF4, and c-MYC) pluripotency markers. Subcutaneously injected DMD hiPSC lines into immunodeficient mice displayed teratoma formation, showing the differentiation capacity into all three developmental germ layers (ectoderm, mesoderm, and endoderm; Figures S1D and S1E). Furthermore, a detailed pluripotency analysis for related genes and proteins is given in the Supplemental information (Figures S1F and S1G). Three control hiPSC lines were used, which were generated from healthy donors with no neuromuscular disorders (Table S1).

CRISPR-Cas9-mediated correction of nonsense mutation in *Dystrophin* gene

Additionally, we created an isogenic control line to exclude genetic background variability. The isogenic control line was generated from DMD patient hiPSCs using CRISPR-Cas9 technology that were characterized by a genetic point mutation in exon 35 (c.4,996C>T; (p.Arg1,666X)) of the *Dystrophin* gene, resulting in a premature stop codon and, consequently, in the complete absence of a functional Dystrophin protein (Figure 1A). To restore the full-length expression of the *Dystrophin* gene, two 20 nt single-guide RNAs (sgRNAs) were designed to induce Cas9-mediated double-stranded breaks (DSBs) in the genomic DNA of the Dystrophin-deficient hiPSCs (Figure 1B). sgRNA specificity and CRISPR-Cas9 DSB cutting were evaluated in HEK293T cells by the appearance of non-homologous end joining (NHEJ) events after transfection of the sgRNA-Cas9 plasmids (Figures S2A and S2B). Cas9-mediated genome editing was performed via homology-directed repair (HDR), using a plasmid-based donor repair template with homology arm regions for the *Dystrophin* gene exon of interest, in order to substitute the premature stop codon into the original amino acid codon for arginine (Figure 1B). Sequencing analysis of exon 35 of the *Dystrophin* gene confirmed CRISPR-Cas9 correction of the DMD hiPSC line, further indicated as DMD isogenic control (Figure 1C). CRISPR-Cas9 off-target events were analyzed based on the sequence homology of sgRNAs (Figure S2C), and detailed comparative genomic hybridization (CGH) molecular karyotyping did not show additional chromosomal abnormalities due to unwanted Cas9-mediated DSB cuts (Figure S2D). To demonstrate that gene editing did not influence the pluripotency state of the DMD isogenic control line, pluripotency genes (*c-MYC*, *GDF-3*, *KLF4*, *NANOG*, *OCT4*, *REX1*, *SOX2*, and *hTERT*) and proteins (OCT4, NANOG, SSEA4, SOX2, TRA-1-60, and LIN28) were analyzed in several undifferentiated human pluripotent stem cell (hPSC) lines (Figures S1F and S1G). Furthermore, immunofluorescent staining showed the expression of the Dystrophin protein (green) in differentiated DMD

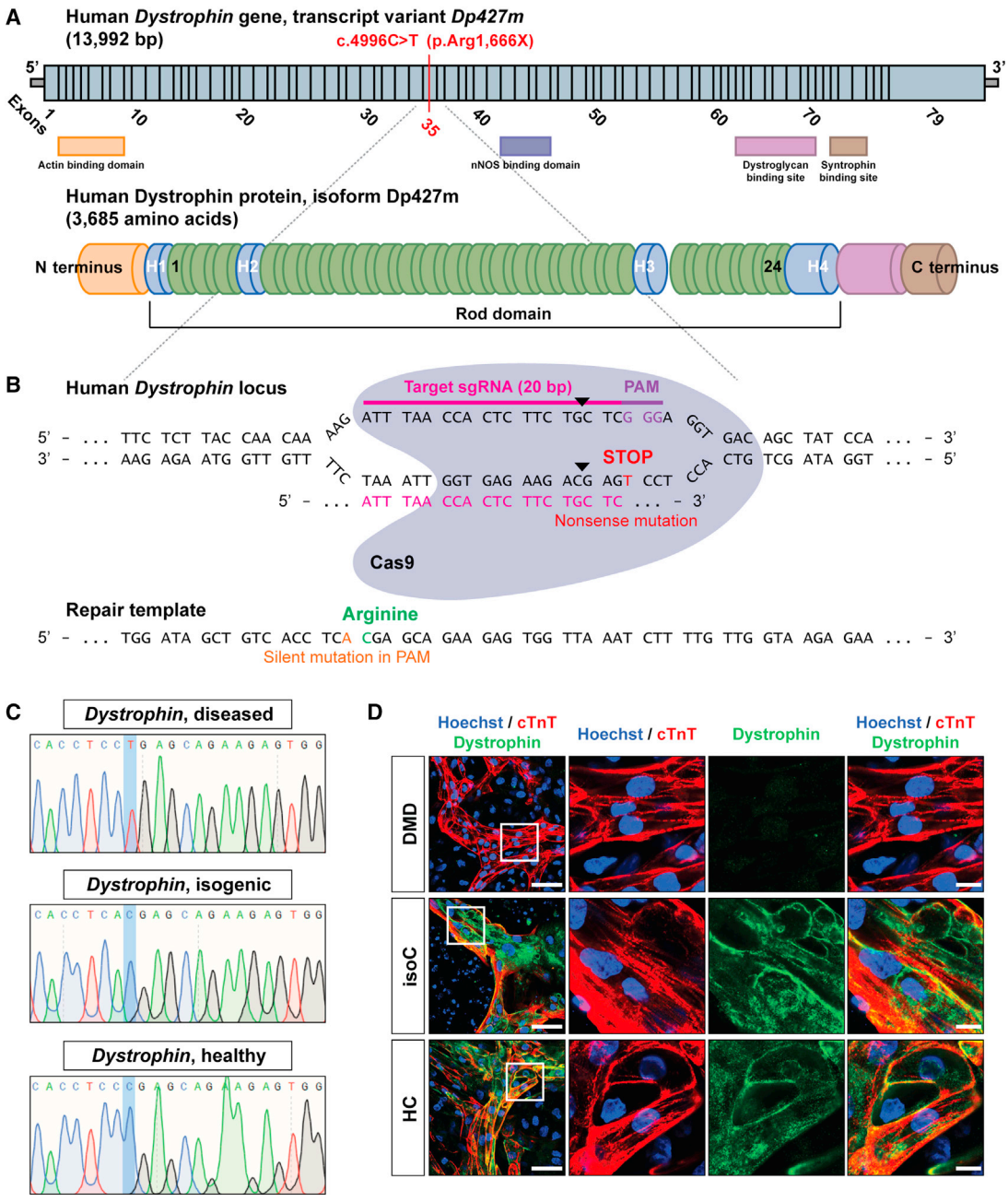

Figure 1. DMD hiPSC CRISPR-Cas9 gene editing of a nonsense mutation in exon 35 (c.4,996C>T; (p.Arg1,666X)) of the *Dystrophin* gene

(A) Schematic representation of the human *Dystrophin* gene sequence (top, transcript variant *Dp427m*) and the encoded Dystrophin protein (bottom, isoform Dp427m). The genetic point mutation is located in exon 35 of the *Dystrophin* gene, resulting in a premature stop codon.

(B) The 20 nt sgRNA (ATTTAACCACTCTTCTGCTC) to induce the Cas9-mediated DSB (indicated as black triangles). The donor repair template containing the genetic correction of the nonsense mutation in the *Dystrophin* gene is also shown.

(C) DNA sequencing of the mutated region of interest of *Dystrophin* before (DMD diseased) and after (DMD isogenic) CRISPR-Cas9 gene editing.

(D) Immunofluorescent staining showing the expression of Dystrophin protein levels (green) in differentiated DMD hiPSC-CMs (cTnT, red and Hoechst, blue) after CRISPR-Cas9-mediated correction. Scale bar: 50 μm. White boxes with corresponding insets are at a higher magnification. Scale bar: 10 μm.

See also Figures S1F, S1G, and S2A–S2D.

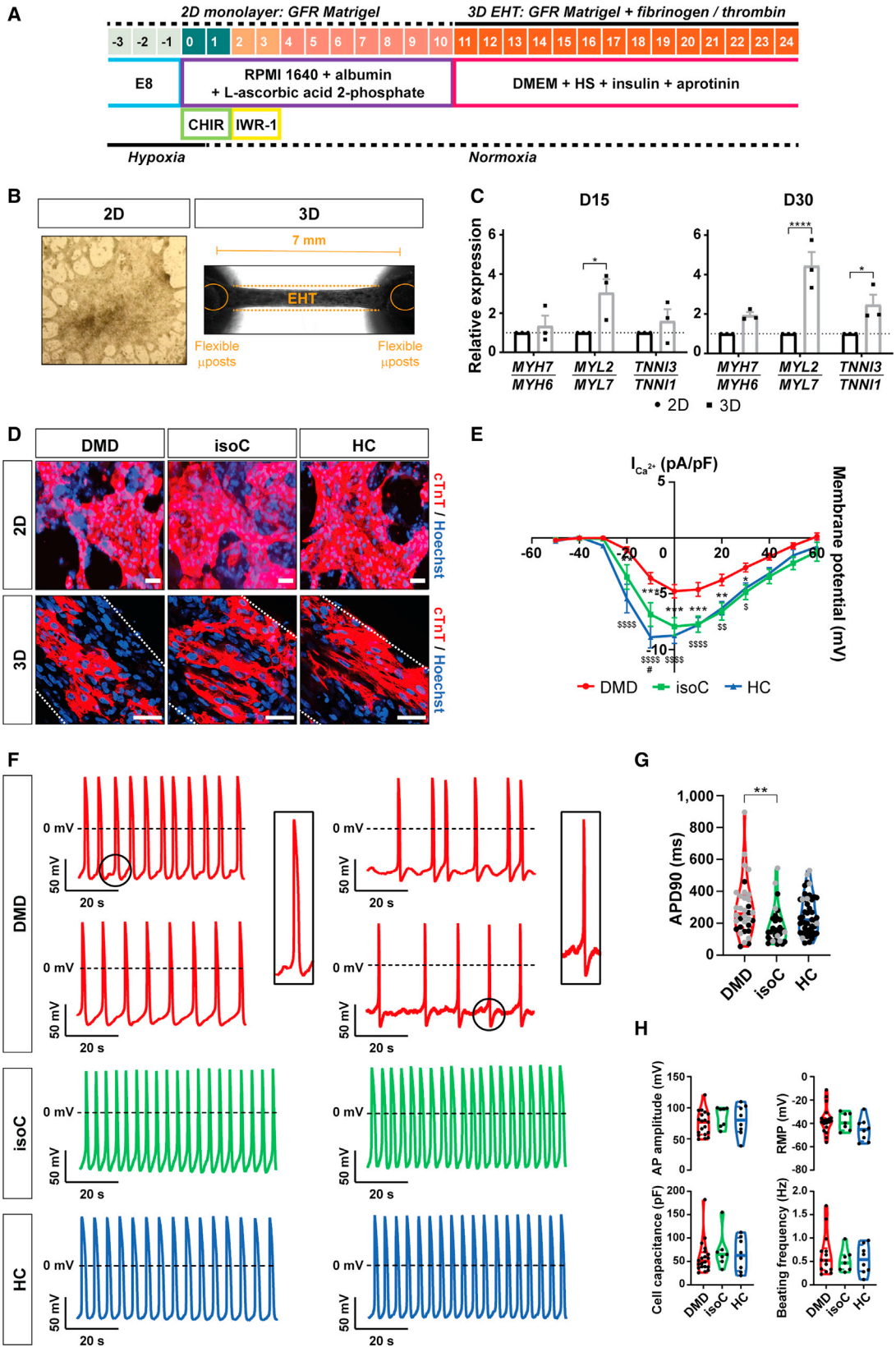

(legend on next page)

hiPSC-CMs (cardiac troponin T [cTnT], red and Hoechst, blue) after CRISPR-Cas9 correction (Figure 1D).

hiPSC-CMs to model diseased heart phenotype in DMD

Burridge et al. developed a fully chemically defined and small-molecule-based cardiac differentiation protocol that is effective for several hiPSC lines and has a high yield of mainly ventricular-like CMs (Burridge et al., 2014). Here, we differentiated control and DMD hiPSC lines to CMs, according to this monolayer-based cardiac differentiation strategy (Burridge et al., 2014), with additional 3D maturation in fibrin-based engineered heart tissue (EHT) constructs (Figures 2A and 2B) (Breckwoldt et al., 2017). During the early phases of cardiac differentiation, hiPSCs were treated with chemical Wnt signaling mediators (CHIR99021 and IWR-1) to obtain high CM yields (Figure 2A). Additional 3D maturation of hiPSC-CMs could significantly increase the expression of the cardiac-specific maturation isoforms *MYL2* and *TNNI3* (Figure 2C). Immunostaining of cTnT-positive hiPSC-CMs additionally matured in 3D EHTs showed a structural, aligned orientation due to the mechanical loading of the flexible microposts compared with those matured in classical 2D monolayer-based differentiation systems (Figure 2D). Importantly, differentiated hiPSC-CMs from DMD patients manifested pathologic features of cardiac involvement. They exhibited a significant reduction of the L-type Ca^{2+} current, indicating abnormal Ca^{2+} homeostasis (Figure 2E), and representative action potential (AP) recordings from DMD hiPSC-CMs displayed arrhythmogenic firing patterns including delayed afterdepolarizations (DADs) and oscillatory prepotentials (OPPs; Figure 2F), as reported in literature (Eisen et al., 2019; Lin et al., 2015; Pioner et al., 2020; Sato et al., 2019). Furthermore, patch-clamp recordings at day 24 of differentiation showed significantly longer mean AP durations at 90% repolarization (APD90) in DMD compared with in control hiPSC-CMs (Figure 2G). Other electrophysiological parameters including AP amplitude, resting membrane potential (RMP), cell capacitance, and beating frequency did not show significant differences (Figure 2H).

Enhanced cell death and excessive intracellular ROS levels in DMD hiPSC-CM cultures

The absence of the Dystrophin protein in differentiated hiPSC-CMs from DMD patients results in the progressive loss of CMs (Davies and Nowak, 2006; Lin et al., 2015). Here, we wanted to identify novel pathological cues that caused decreased cell survival of DMD hiPSC-CMs. We mainly used DMD hiPSCs that were characterized by the nonsense mutation in exon 35 (c.4,996C>T; (p.Arg1,666X)) of the *Dystrophin* gene (DMD #2 in Table S1). This DMD line represents a subgroup of DMD patients (approximately 13%) that is responsive to the readthrough chemical drug ataluren (PTC124; Figures 3A–3C). Cell death was examined by flow cytometric analyses using annexin V and 7-amino-actinomycin D (7AAD). DMD hiPSC-CMs underwent accelerated cell death compared with corresponding DMD isogenic and healthy controls (Figures 4A and S3A, left panels). A remarkable percentage of DMD hiPSC-CMs had high intracellular ROS concentrations compared with those found in controls (Figures 4B and S3A, middle panels). Moreover, the intracellular ROS content (mean fluorescence intensity [MFI]) in DMD hiPSC-CMs was

Figure 2. Characterization of the hiPSC-CM differentiation protocol

(A) Schematic representation of the cardiac differentiation protocol. hiPSCs were differentiated to CMs in a monolayer cardiac differentiation protocol using chemical Wnt signaling mediators (CHIR99021 and IWR-1) and, eventually, further matured into 3D EHT constructs based on fibrinogen and thrombin polymerization.

(B) Representative example of 2D monolayer-based cardiac differentiation (left panel) and 3D mini-EHT construct between two flexible microposts positioned 7 mm from each other (right panel).

(C) Normalized gene expression ratios for isoforms of *Myosin Heavy Chain* (*MYH7/MYH6*), *Myosin Light Chain* (*MYL2/MYL7*), and *Cardiac Troponin I* (*TNNI3/TNNI1*) after 15 and 30 days of differentiation. Data are representative of three independent experiments (n = 3), and values are expressed as mean ± SEM. Significance of the difference is indicated as follows: *p < 0.05, **p < 0.01, ***p < 0.001, and ****p < 0.0001.

(D) Immunostaining of cardiac troponin T (cTnT) -positive CMs (cTnT, red and Hoechst, blue) in monolayer-based cardiac differentiation (2D) or EHT constructs (3D). White dotted lines indicate the borders of the 3D EHT constructs. Scale bar: 50 μm.

(E) Voltage-current relation curve of the L-type Ca^{2+} current (pA/pF) assessed after whole-cell patch-clamp configuration. Each data point indicated biological replicates (DMD: N = 13, DMD isogenic: N = 7, healthy: N = 11), and values are expressed as mean ± SEM. *p < 0.05, **p < 0.01, ***p < 0.001, and ****p < 0.0001 (DMD versus DMD isogenic control) or $^{\$}$p < 0.05, $^{\$\$}$p < 0.01, $^{\$\$\$}$p < 0.001, and $^{\$\$\$\$}$p < 0.0001 (DMD versus healthy control).

(F) Representative AP recordings. DMD hiPSC-CMs displayed arrhythmogenic firing patterns including DADs and OPPs.

(G) Patch-clamp recordings at day 24 of differentiation for mean APD90 (ms). Additional measurements were performed with di-4-ANEPPS (gray dots).

(H) Patch-clamp recordings for AP amplitude (mV), RMP (mV), cell capacitance (pF), and beating frequency (Hz). Each data point indicates biological replicates (DMD: N = 19, DMD isogenic: N = 7, healthy: N = 8). *p < 0.05, **p < 0.01, ***p < 0.001, and ****p < 0.0001.

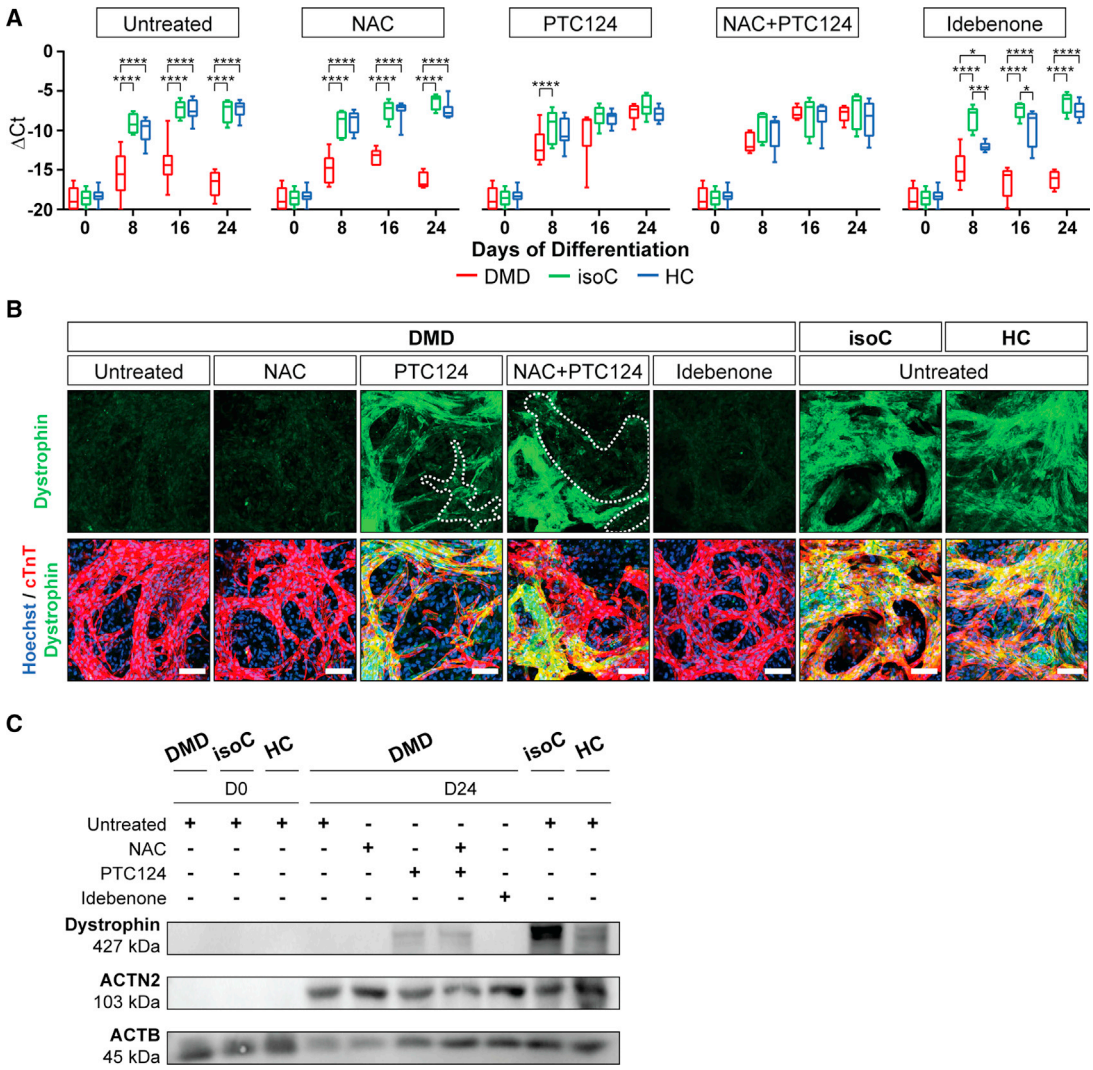

Figure 3. Dystrophin re-expression in DMD hiPSC-CMs after PTC124 treatment

(A) *Dystrophin* gene expression profiles in DMD hiPSC-CMs, characterized by a genetic point mutation in exon 35 (c.4,996C>T; (p.Arg1,666X)) of the *Dystrophin* gene, upon NAC, PTC124, and idebenone addition. Each data point is represented as ΔCt and normalized for the housekeeping genes (*GAPDH* and *RPL13a*). Data are representative of five or more independent experiments ($n \geq 5$), and values are expressed as mean ± SEM. *$p < 0.05$, **$p < 0.01$, ***$p < 0.001$, and ****$p < 0.0001$ versus subjects within the treatment condition.

(B) Immunostaining at day 24 of differentiation demonstrating Dystrophin protein re-expression (green) upon PTC124 treatment in cTnT-positive DMD and control hiPSC-CMs (cTnT, red and Hoechst, blue). Scale bar: 100 μm.

(C) Western blot analysis quantifying Dystrophin proteins in ACTN2-positive DMD and control hiPSC-CMs, normalized to the loading protein ACTB.

significantly higher (Figures 4C and S3A, right panels). Upon treatment with NAC, PTC124 (alone or in combination), or idebenone, DMD hiPSC-CMs showed increased cell survival (Figures 4A and S3A, left panels) and reduced intracellular ROS levels (Figures 4B and S3A, middle panels) compared with those in untreated DMD hiPSC-CMs. The specificity of the drug effect on CM death and intracellular ROS levels of the experimental groups is shown in the Supplemental information (Figures S4A–S4D). Taken together, these results show increased intracellular ROS levels in DMD hiPSC-CMs. Interestingly, NAC, PTC124, and idebenone had beneficial effects on the cell survival, although idebenone exhibited superior effects in DMD cultures.

Dystrophin-deficient hiPSC-CMs are characterized by depolarized mitochondria

DMD pathology is accompanied by abnormal intracellular Ca^{2+} handling and the accumulation of

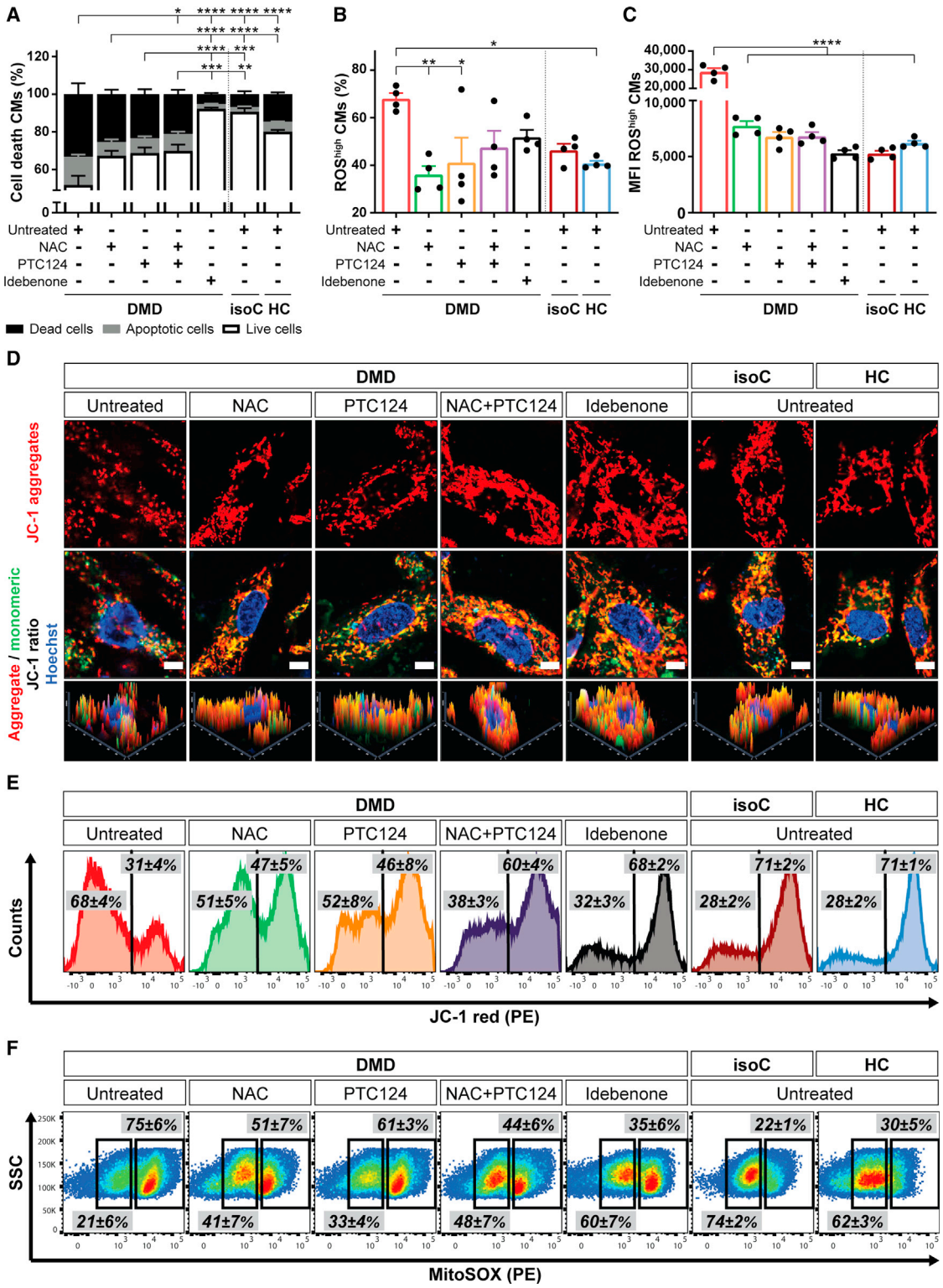

Figure 4. Characterization of the cardiomyopathic phenotype *in vitro* of DMD hiPSC-CMs, showing premature cell death, depolarized mitochondria, and increased intracellular ROS levels, which were counteracted by NAC, ataluren (PTC124), and idebenone

(A–C) Flow cytometric quantification at day 15 of cardiac differentiation showing the percentage of cell death of signal-regulatory protein alpha (SIRPA)-positive hiPSC-CMs (A), the percentage of CMs with high intracellular ROS levels (B), and the MFI of intracellular ROS in CMs

(legend continued on next page)

dysfunctional mitochondria with defective structures (Timpani et al., 2015). A distinctive feature of early phase cell death is the loss of the membrane potential of active mitochondria ($\Delta\Psi_m$) (Zorova et al., 2018). The carbocyanine compound JC-1, a fluorescent voltage-sensitive dye with membrane-permeant fluorescent lipophilic cationic properties (Mathur et al., 2000), was used to determine $\Delta\Psi_m$ and mitochondrial health. Consistently with the previously observed accelerated death of untreated DMD hiPSC-CMs, these cultures were characterized by mitochondrial depolarization, indicated by the decrease in the red (aggregates)/green (monomers) JC-1 fluorescence intensity ratio (Figures 4D, 4E, and S3B). Interestingly, the combinatorial treatment of NAC and PTC124, as well idebenone treatment, displayed significantly beneficial effects on $\Delta\Psi_m$ with respect to untreated DMD hiPSC-CMs. Furthermore, flow cytometric analyses confirmed a significant increased superoxide production in depolarized mitochondria compared with in controls (Figures 4F and S3C). No significant differences were observed for mitochondrial content upon the different treatments (Figures S3D and S3E). The specificity of the drug effect on $\Delta\Psi_m$ and on the mitochondrial superoxide concentrations of the experimental groups is shown in the Supplemental information (Figures S4E–S4H). Taken together, these results indicate dysfunctional depolarized mitochondria in DMD hiPSC-CMs, which could lead to excessive ROS leakage. The combined treatment of NAC and PTC124, as well idebenone treatment, could rescue this condition.

NOX4 is overexpressed in DMD hiPSC-CMs

Several independent studies have reported increased NOX4 expression and activity in chronic heart failure, supporting the clinical relevance, although the role of NOX4 in CMs is still unclear (Ago et al., 2010; Spurney et al., 2008; Varga et al., 2017; Zhang et al., 2013). Here, NOX2 and NOX4, the predominantly expressed isoforms of the ROS-producing NOX family enzymes in the heart, were investigated. Gene expression profiles did not reveal a differential expression for *NOX2* and accessory regulatory subunits ($p47^{phox}$, $p67^{phox}$, *RAC2*, and *RAC3;* Figure 5A). Interestingly, *NOX4* and its regulatory subunit $p22^{phox}$ were significantly upregulated in DMD hiPSC-CMs. Moreover, DMD hiPSC-CMs treated with PTC124 alone or in combination with NAC exhibited decreased *NOX4* and $p22^{phox}$ gene levels. In contrast, upon idebenone treatment, no reduction was observed in the expression of both genes. Flow cytometric analyses demonstrated a significant increased percentage of NOX4-positive DMD hiPSC-CMs compared with DMD isogenic and healthy controls (Figures 5B and 5C). The percentage of NOX4-positive DMD hiPSC-CMs was reduced upon idebenone treatment. The specificity of the drug on the expression of NOX4 among the experimental groups is shown in the Supplemental information (Figures S4I and S4J). Western blot analysis confirmed the increased protein levels of NOX4 in DMD hiPSC-CMs (Figure 5D). Upon idebenone addition, DMD hiPSC-CMs showed a downregulation of NOX4, as also observed in controls. These data demonstrate a significantly increased NOX4 expression in DMD hiPSC-CMs that upon treatment with idebenone could be reverted to basal levels.

Additionally, we demonstrated that the NOX4 upregulation in DMD hiPSC-CMs (DMD #2 in Table S1) was not a common downstream pathway of cell death. Therefore, we preincubated hiPSC-CMs with 1 μM staurosporine (STS), a potent cell death inducer, for 6 h (Belmokhtar et al., 2001), and we did not observe any increase in the NOX4 expression (Figures S5A and S5B). Interestingly, by analyzing $\Delta\Psi_m$ and the mitochondrial superoxide production in various DMD-patient-specific hiPSC-CM lines (DMD #2, DMD #5, and DMD #6 in Table S1), we could observe an association between the levels of mitochondrial depolarization and ROS production with the gene and protein levels of NOX4, suggesting a crucial role of NOX4 (Figures S6A–S6G).

(C) in conditions with (NAC, PTC124, and idebenone) or without (untreated) treatments. Data are representative of four independent experiments (n = 4), and values are reported as mean ± SEM. *p < 0.05, **p < 0.01, ***p < 0.001, and ****p < 0.0001.

(D) Immunostaining of the fluorescent voltage-sensitive dye JC-1 was used to determine $\Delta\Psi_m$ and mitochondrial health in 15-day-old differentiated hiPSC-CMs. Untreated DMD hiPSC-CMs were characterized by mitochondrial depolarization, as indicated by the decrease in mitochondrial aggregates (JC-1 red, top panels) and the increase in mitochondrial monomers (JC-1 green, middle panels) with respect to treated DMD hiPSC-CMs and controls. Corresponding histograms (bottom panels) showed the JC-1 fluorescence intensity ratios (aggregates/monomers). Scale bar: 5 μm.

(E) Representative flow cytometric analyses at day 15 of differentiation for JC-1 aggregates (phycoerythrin [PE]) and JC-1 monomers (fluorescein isothiocyanate [FITC]) in DMD hiPSC-CMs upon treatment. Data are representative of four independent experiments (n = 4).

(F) Flow cytometric analyses at day 15 of differentiation showing the mitochondrial superoxide production (MitoSOX; PE) in depolarized DMD mitochondria compared with in DMD isogenic and healthy controls. Data are representative of four independent experiments (n = 4). Flow cytometry data are reported as mean ± SEM.

See also Figures S3A–S3E and S4A–S4H.

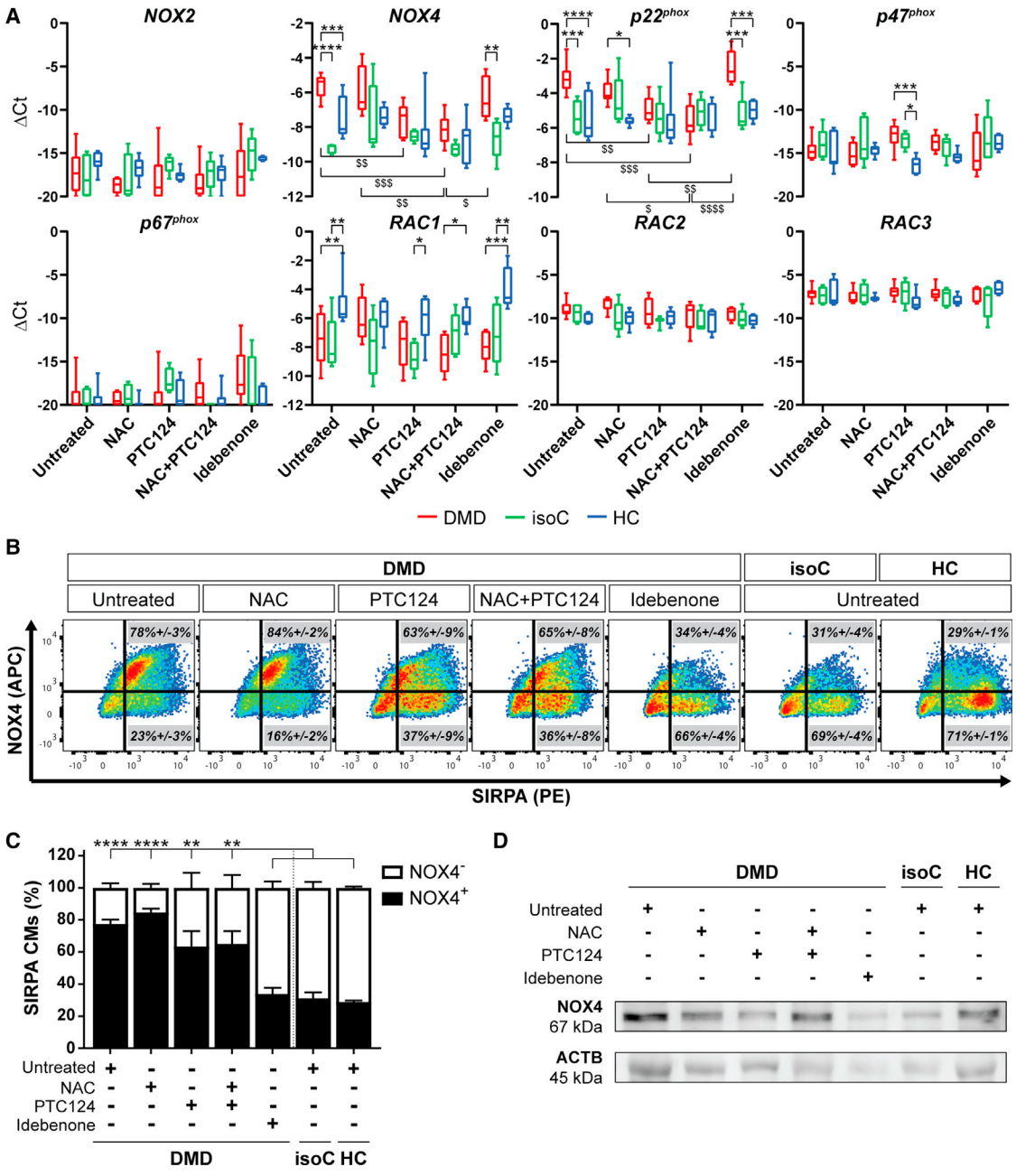

Figure 5. Increased expression levels of the ROS-producing NOX family enzyme NOX4 and its accessory regulatory subunit p22^{phox} in Dystrophin-deficient hiPSC-CM cultures

(A) Gene expression profiles at day 24 of cardiac differentiation of *NOX2* and *NOX4*, and the regulatory subunits (*p22^{phox}*, *p47^{phox}*, *p67^{phox}*, *RAC1*, *RAC2*, and *RAC3*) in DMD, DMD isogenic, and healthy control hiPSC-CMs upon treatment with NAC, PTC124, and idebenone. Each data point is represented as ΔCt and is normalized for the housekeeping genes (*GAPDH* and *RPL13a*). Data are representative of five or more independent experiments ($n \geq 5$), and values are expressed as mean ± SEM. *$p < 0.05$, **$p < 0.01$, ***$p < 0.001$, and ****$p < 0.0001$ versus subjects within the treatment condition or $^{\$}p < 0.05$, $^{\$\$}p < 0.01$, $^{\$\$\$}p < 0.001$, and $^{\$\$\$\$}p < 0.0001$ versus treatment conditions within the subject group.

(B) Representative flow cytometric analyses at day 15 of differentiation showing the percentage of NOX4 (APC) protein expression in SIRPA (PE)-positive DMD hiPSC-CMs upon treatment. Data are representative of three independent experiments (n = 3). Flow cytometry data are reported as mean ± SEM.

(legend continued on next page)

Idebenone stimulates ATP production in depolarized mitochondria, ameliorating NOX4-mediated ROS overproduction

Overall, oxidative stress, in synergy with intracellular Ca^{2+} overload, results in the progressive worsening of DMD cardiomyopathy (Allen et al., 2016). We hypothesized that *Dystrophin* gene mutations elicit excessive ROS generation via the mitochondrial ETC of depolarized mitochondria and via a NOX4-based NADPH-dependent process. To assess whether increased NOX4 could contribute to elevated intracellular ROS concentrations, *NOX4* mRNA levels were transiently degraded by the addition of Antisense LNA GapmeRs to the DMD hiPSC-CM cultures (Figure 6A, left panel). Antisense LNA GapmeRs targeting *MALAT1* mRNA were used as positive controls (Figure 6A, right panel). Interestingly, transient GapmeR-induced *NOX4* mRNA degradation significantly reduced NOX4 activity, as monitored through changes in NADPH absorption (Figure 6B) (Shanmugasundaram et al., 2017). DMD hiPSC-CMs exhibited significantly elevated NOX4 activity compared with controls (Figure 6C). However, when idebenone was added to DMD hiPSC-CM cultures, the NOX4 NADPH-dependent ROS production was significantly reduced in isolated mitochondria (Figure 6C) and in the total CM fraction (Figure S7A). Moreover, idebenone restored ATP levels due to its electron donating property for mitochondrial ETC stimulation (Figures 6D and S7B).

Recent studies have identified an ATP-binding motif within NOX4 through which ATP, upon binding, could regulate NOX4 activity (Shanmugasundaram et al., 2017). Adding dose-dependent ATP concentrations to DMD hiPSC-CM cultures demonstrated that 2.5 mM ATP had a beneficial effect and significantly reduced ROS production of the NOX4 activity with respect to no ATP addition (Figures 6E and S7C). Interestingly, idebenone alone or in combination with a 2.5 mM ATP addition did ameliorate the activity of NOX4 in a similar manner, resulting in a significantly decreased NADPH-dependent ROS production compared with untreated DMD hiPSC-CMs (Figures 6F and S7D). The specificity of idebenone on the NOX4 ROS-producing activity and on the ATP levels of the experimental groups is shown in the Supplemental information (Figures S7E–S7H). These findings reveal an increased mitochondrial ROS-producing NOX4 activity in DMD hiPSC-CMs, which was counteracted by idebenone through ATP.

DMD EHTs show improved contractile function after idebenone administration

In order to assess the amplitude of contraction of 3D EHT constructs, we monitored the micropost deflection movements of the EHT devices, which were the result of a spontaneous contraction of the EHTs attached to the flexible microposts (Figure 2B). At physiological 1.8 mM Ca^{2+} concentrations, the contractile function of untreated DMD hiPSC-CM EHTs was significantly lower than of untreated EHTs generated from isogenic or healthy hiPSC-CMs (Figure 7A), confirming the validity of the 3D EHT model system for DMD. However, DMD EHTs treated with idebenone exhibited a significantly increased contraction, whereas the combined treatment of idebenone and PTC124 improved the contractile function even further. By incubating DMD EHTs with Ca^{2+} concentrations of 2.5 mM, we wanted to analyze the amplitude of contraction of DMD EHTs, mimicking the detrimental increased Ca^{2+} environment, as reported in hearts from DMD patients (Figure 7B) (Kyrychenko et al., 2017; Sato et al., 2019). At higher Ca^{2+} concentrations, treatment with idebenone alone no longer improved the contractile function of DMD EHTs. However, the contractile function remained significantly improved with the combinatorial treatment of idebenone and PTC124. These data point out the beneficial effect of a combinatorial treatment of idebenone and PTC124, highlighting the importance of targeting simultaneously different aspects of DMD cardiomyopathy in terms of heart functionality.

DISCUSSION

hiPSCs have the potential to differentiate in functional cell types that can be used as an unlimited cell source of inaccessible tissues to study genetic disorders and, consequently, to gain novel insights in signaling pathways involved in the disease pathology.

In this study, we generated hiPSC-based cardiac disease models from three DMD patients to study the early stages of cardiomyopathy in DMD. hiPSCs were differentiated toward CMs according to the protocol of Burridge et al. (Burridge et al., 2014) and Breckwoldt et al. (Breckwoldt et al., 2017). First, hiPSCs were differentiated in a monolayer-based method using a fully chemically defined medium consisting of the basal medium RPMI 1640, rice-derived

(C) Flow cytometric quantification at day 15 of differentiation of the percentage of SIRPA-positive hiPSC-CMs expressing NOX4 upon treatment. Data are representative of three independent experiments (n = 3), and values are expressed as mean ± SEM. *p < 0.05, **p < 0.01, ***p < 0.001, and ****p < 0.0001.

(D) Western blot analysis quantifying the protein expression levels of NOX4 in 15-day-old differentiated DMD and control hiPSC-CMs, normalized to the loading protein ACTB. See also Figures S4I and S4J.

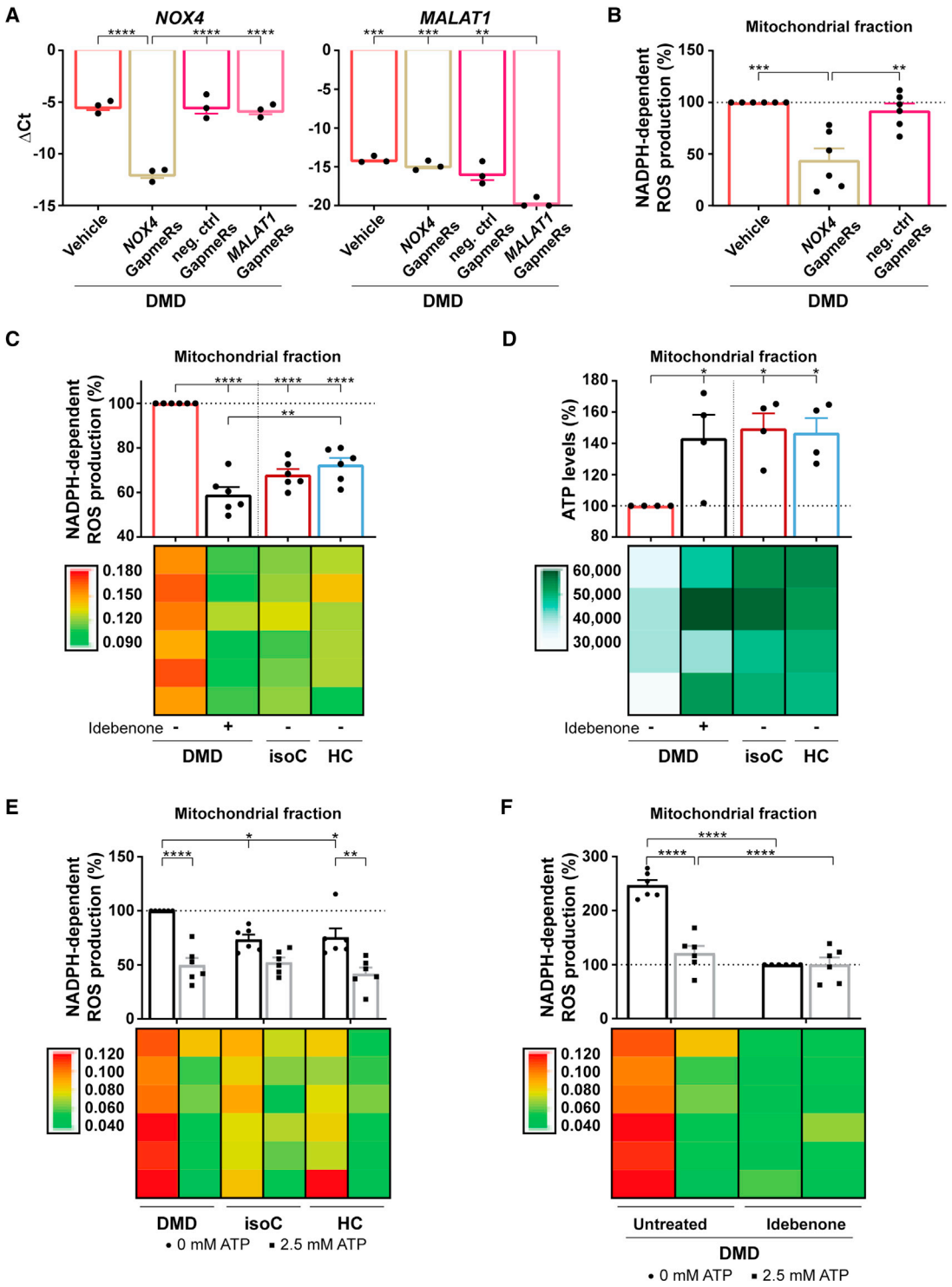

Figure 6. Idebenone could counteract the oxidative stress in DMD hiPSC-CMs through ATP stimulation of the mitochondrial ETC, which, in turn, reduced ROS-producing NOX4 activity

(A) Quantitative RT-PCR of *NOX4* gene expression levels after the addition of NOX4-targeted Antisense LNA GapmeRs to the DMD hiPSC-CM cultures (left panel). As a positive control for the efficiency of the Antisense LNA GapmeRs, *MALAT1* levels were determined after the addition of MALAT1-targeted Antisense LNA GapmeRs (right panel). Each data point is represented as ΔCt and is normalized for the

(legend continued on next page)

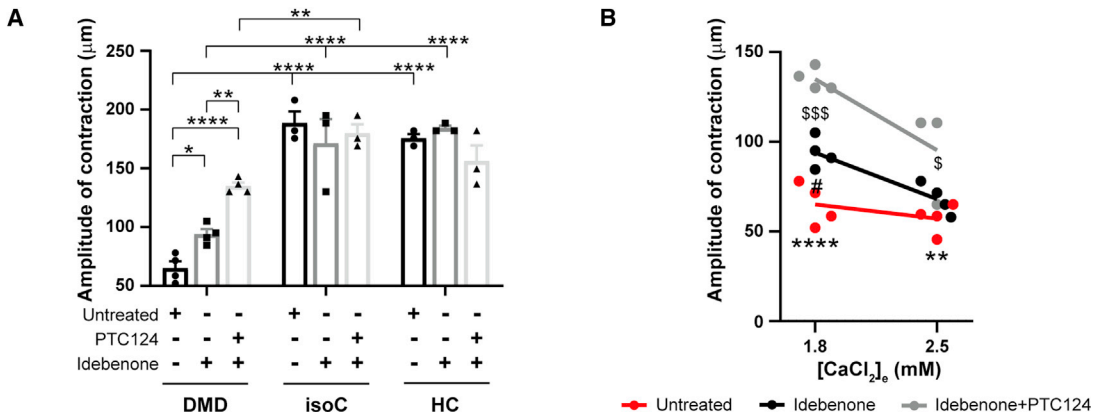

Figure 7. Improved contraction of 3D EHT constructs after administration of idebenone alone or in combination with PTC124 under physiological Ca^{2+} levels

(A) Spontaneous contraction and relaxation cycles of EHTs were monitored under temperature-controlled conditions (37°C) at 1.8 mM physiological Ca^{2+} concentrations and measured by the deflection movements of the microposts (in µm). The effect of idebenone and PTC124 on the contractility of EHTs derived from DMD hiPSC-CMs (EHT diameter: 1,041.9 ± 74.1 µm) was compared with that from DMD isogenic (diameter: 938.0 ± 86.6 µm) and healthy control EHTs (diameter: 849.9 ± 80.5 µm). Data are representative of three or four independent experiments ($n \geq 3$), and values are expressed as mean ± SEM. *$p < 0.05$, **$p < 0.01$, ***$p < 0.001$, and ****$p < 0.0001$.

(B) EHTs derived from DMD hiPSC-CMs were incubated with Ca^{2+} concentrations of 1.8 and 2.5 mM to assess the amplitude of contraction. Data are representative of three or four independent experiments ($n \geq 3$), and values are expressed as mean ± SEM. *$p < 0.05$, **$p < 0.01$, ***$p < 0.001$, and ****$p < 0.0001$ (untreated versus idebenone + PTC124), $^{\$}p < 0.05$, $^{\$\$}p < 0.01$, $^{\$\$\$}p < 0.001$, and $^{\$\$\$\$}p < 0.0001$ (idebenone versus idebenone + PTC124), or $^{\#}p < 0.05$, $^{\#\#}p < 0.01$, $^{\#\#\#}p < 0.001$, and $^{\#\#\#\#}p < 0.0001$ (untreated versus idebenone).

recombinant human albumin, and L-ascorbic acid 2-phosphate along with a small-molecule-based induction of differentiation (Burridge et al., 2014). L-ascorbic acid 2-phosphate has been shown to enhance cardiac differentiation and maturation through increased collagen production by promoting cardiac progenitor cell proliferation via the MEK-ERK1/2 pathway. Furthermore, L-ascorbic acid 2-phosphate-induced CMs exhibited better sarcomeric organization and enhanced responses of APs and Ca^{2+} transients to β-adrenergic and muscarinic stimulations (Cao et al., 2012). Second, hiPSC-CMs were further differentiated in 3D fibrin-based EHT constructs for contractility measurements (Breckwoldt et al., 2017). In several cancer-related studies, the effect of ascorbic acid on ROS production has been reported (Fukumura et al., 2012; Wei et al., 2017). In these studies, a ROS-scavenger effect was observed after the addition of 1 mM or higher concentrations of ascorbic acid. We used a lower final concentration, suggesting no significant antioxidative effect on ROS levels. Interestingly, Bartsch et al. (Bartsch et al., 2011) demonstrated an ascorbic-acid-enhanced cardiac differentiation accompanied by an upregulation of the NADPH

housekeeping genes (*GAPDH* and *RPL13a*). Data are representative of three independent experiments (n = 3), and values are expressed as mean ± SEM. *$p < 0.05$, **$p < 0.01$, ***$p < 0.001$, and ****$p < 0.0001$.

(B) Quantification of the NOX4 ROS production, measured via the NADPH-dependent ROS generation, in the isolated mitochondrial fraction of DMD hiPSC-CMs after a 6-day preincubation with GapmeRs. Each data point is represented as a percentage (%) and is normalized to the mitochondrial fraction of the untreated DMD hiPSC-CMs (vehicle).

(C) Quantification of the NADPH-dependent ROS production of NOX4 in the mitochondrial fraction of DMD hiPSC-CMs with or without idebenone treatment compared with in DMD isogenic and healthy controls.

(D) ATP luminescence detection showing the effect of idebenone treatment on the mitochondrial ATP levels in DMD hiPSC-CMs.

(E) Quantification of the ROS-producing NOX4 activity after 2.5 mM ATP addition in DMD hiPSC-CM and control cultures. Each data point is represented as a percentage (%) and is normalized to the mitochondrial fraction of the untreated DMD hiPSC-CMs.

(F) Quantification of the NADPH-dependent ROS production of NOX4 in the mitochondrial fraction of DMD hiPSC-CMs upon 2.5 mM ATP addition with or without idebenone treatment. Each data point is represented as a percentage (%) and is normalized to the mitochondrial fraction of the idebenone-treated DMD hiPSC-CM cultures. Data are representative of four or six independent experiments (n = 4 or n = 6), and values are expressed as mean ± SEM. *$p < 0.05$, **$p < 0.01$, ***$p < 0.001$, and ****$p < 0.0001$. Colored rectangles represent the independent experiments.

See also Figures S7A–S7H.

oxidase isoforms NOX2 and NOX4 at basal expression levels with intracellular physiological ROS concentrations, indicating the suitability of the applied cardiac differentiation methods.

hiPSC-CMs obtained from DMD patients represent hallmarks of DMD-associated heart complications in *in vitro* cultures. Published studies showed that the lack of Dystrophin in DMD hiPSC-CMs resulted in enhanced cell death (Lin et al., 2015), Ca^{2+}-handling abnormalities, and reduced contractile function (Kyrychenko et al., 2017; Sato et al., 2019). We observed premature cell death of DMD hiPSC-CMs due to significantly elevated intracellular oxidative stress levels. Furthermore, a detailed characterization demonstrated mitochondrial depolarization and significantly increased NOX4 expression. Whether the abnormal upregulation of NOX4 and its increased basal rate of ROS production are a direct or indirect consequence of the absence of Dystrophin is currently unknown. Increased Nox4 proteins have been found in left ventricular CMs of *mdx* mice and are associated with fibrosis and altered functional parameters in the heart (Spurney et al., 2008). Deep RNA sequencing of the cardiac transcriptome on explanted human heart samples, obtained from patients suffering from heart failure, indicated extensive alternative splicing of the *NOX4* gene, which is associated with upregulation of the full-length NOX4 protein (Varga et al., 2017). Consistent with these results, we found significantly increased expression and activity of the cardiac-specific ROS-producing NOX4 isoform in DMD hiPSC-CMs. Dystrophin-deficient CMs are more vulnerable to mechanical stress due to their increased membrane fragility and stretch-induced Ca^{2+} influx, which results in cell death (Kyrychenko et al., 2017; Lin et al., 2015; Sato et al., 2019). The complexity of the DMD pathology results from signal amplification systems with bidirectional crosstalk and positive feedback loops. ROS generation in response to mechanical forces may originate from diverse sources including mitochondria and NOX isoforms (Ago et al., 2010; Zhang et al., 2013) or even other oxidase systems (Kerr et al., 2015; Khairallah et al., 2012; Prosser et al., 2011).

To ameliorate the DMD disease phenotype, we applied several therapeutic approaches. We investigated whether NAC, ataluren (PTC124), and idebenone could have beneficial effects on the dystrophic features observed in DMD hiPSC-CM cultures. PTC124 drug efficacy analyses were performed only on DMD hiPSCs with the nonsense mutation in exon 35 (c.4,996C>T; (p.Arg1,666X)) of the *Dystrophin* gene. This line represents a subgroup of DMD patients (approximately 13%) that is responsive to the readthrough chemical drug PTC124, which allowed us to investigate the effects of PTC124 on DMD cardiomyopathy in an *in vitro* hiPSC-based disease model. PTC124 is one of the gene-based therapeutic approaches for DMD, although it is applicable for only a small subgroup of DMD patients with a nonsense mutation (Welch et al., 2007). We demonstrated re-expression of Dystrophin after PTC124 addition in a fraction of differentiating DMD hiPSC-CMs. Recently, a phase 3 randomized, placebo-controlled trial evaluating an improvement in the 6-min walking test after 48 weeks has been completed (Campbell et al., 2020), and a clinical trial to study Dystrophin expression levels in a small cohort of PTC124-treated patients with DMD is currently ongoing. These clinical studies aim at targeting the primary cause of DMD progression.

Nowadays, several innovative therapeutic approaches focus on secondary pathology. In the last decade, researchers have shown growing interest in idebenone as potential treatment for DMD. The precise mechanism by which idebenone exerts its protective effect is still unknown. Yet, idebenone has been reported to protect mitochondria from oxidative damage and to boost their impaired function, delaying the disease progression of DMD (Buyse et al., 2015). Interestingly, given the dual mode of action of idebenone (ROS-scavenger function and stimulation of the mitochondrial ETC), we showed that idebenone exhibited a superior beneficial outcome on DMD hiPSC-CMs through increased ATP production that, in turn, decreased NOX4 activity. The exact mechanism of ATP-mediated inhibition of NOX4 activity is still unclear.

Recently, an ATP-binding motif within the NOX4 isoform has been identified, suggesting a potential novel mechanism through which NOX4 can be allosterically regulated. During normal respiration, OXPHOS-driven ATP production in the mitochondria binds NOX4 through the ATP-binding domain, keeping the NOX4-produced ROS levels low (Shanmugasundaram et al., 2017). The ATP-binding motif (AXXXXGKT) (Walker et al., 1982) that resides within the amino acids 534–541 of the C terminus, is unique to NOX4 (it is not found in other NOX isoforms) and is conserved in *Homo sapiens*, *Rattus norvegicus*, and *Mus musculus* (Shanmugasundaram et al., 2017). In line with these results, we demonstrated that the addition of idebenone to DMD hiPSC-CM cultures increased the intracellular and, more specifically, the mitochondrial ATP concentrations through idebenone-induced ETC stimulation. Moreover, idebenone could significantly reduce the ROS-producing NOX4 activity, assuming the allosterically regulation of NOX4 through ATP. Interestingly, the addition of external ATP to DMD hiPSC-CM cultures resulted in a similar reduction of the NADPH-dependent ROS production of NOX4.

Elevated ATP concentrations can be used by skeletal and cardiac myosin to increase cross-bridge binding and cycling, leading to stronger and faster contraction and relaxation

(Moussavi-Harami et al., 2015). Cardiac-specific overexpression of the enzyme ribonucleotide reductase that converts adenosine diphosphate (ADP) to deoxy-ADP (dADP), which, in turn, is rapidly converted to deoxy-ATP (dATP) in cells, facilitated CM contraction and cardiac performance in normal rodent hearts and in rodent and pig infarcted hearts (Kolwicz et al., 2016). We showed improved contractile properties of EHTs derived from DMD hiPSC-CMs upon idebenone administration at physiological Ca^{2+} concentrations. Preincubation of idebenone with PTC124 further enhanced the contractility, probably due to the PTC124-induced re-expression of Dystrophin proteins. In line with these results, the Olson's group performed CRISPR-Cas9-mediated exon skipping ("myoediting") for DMD mutation corrections in order to rescue the contractile dysfunction of DMD hiPSC-CMs that were differentiated in 3D EHTs (Atmanli et al., 2021; Kyrychenko et al., 2017).

In conclusion, by using DMD-patient-derived hiPSC-CMs, we provided the first evidence that NOX4 expression and activity were significantly upregulated, contributing to increased intracellular ROS and cell death. Furthermore, we compared the effects of NAC, PTC124, and idebenone in an *in vitro* setting of cardiomyopathic DMD. Finally, we gained novel mechanistic insights into the mode of action of idebenone on the hyperactive state of NOX4 ROS production. Idebenone-mediated stimulation of ATP production by the ETC of mitochondria could increase the affinity of ATP to bind with NOX4, reducing its ROS production. Considering the early cellular stress responses present in CMs from DMD patients, interfering with any of these early cellular events that lead to excessive ROS signals would positively affect the mitochondrial activity, resulting in an improved contractile function.

EXPERIMENTAL PROCEDURES

hiPSC culture

Control and DMD-diseased hiPSC lines (Table S1) were cultured feeder-free on Geltrex LDEV-Free hESC-Qualified Reduced Growth Factor Basement Membrane Matrix and maintained in Essential 8 Flex Basal Medium supplemented with Essential 8 Flex Supplement (50×) and 0.1% penicillin-streptomycin (Pen/Strep) (all from Thermo Fisher Scientific) at 37°C under normoxic conditions (21% O_2 and 5% CO_2). Colonies were routinely passaged non-enzymatically with 0.5 mM EDTA in phosphate-buffered saline (PBS; both from Thermo Fisher Scientific). Mycoplasma contamination was assessed on a periodic basis for all cell cultures. No contaminated cells were used in the described experiments of this study.

Monolayer-based cardiac differentiation of hiPSCs

hiPSCs were differentiated into functional CMs according to a monolayer-based cardiac differentiation protocol, as previously described (Burridge et al., 2014). Briefly, prior to differentiation, control and DMD hiPSC lines were split into small colonies and subsequently cultured on a thin Matrigel Growth Factor Reduced (GFR) Basement Membrane Matrix layer (Corning) in complete Essential 8 flex medium at 37°C under hypoxic conditions (5% O_2 and 5% CO_2), in order to obtain the optimal confluency of 85%, 3 days after splitting. Mesoderm differentiation (day 0) was induced using 6 μM CHIR99021 (Axon Medchem) for 48 h in a chemically defined medium consisting of RPMI 1640 (Thermo Fisher Scientific), 500 μg/mL rice-derived recombinant human albumin, and 213 μg/mL L-ascorbic acid 2-phosphate (both from Merck). After 24 h of CHIR99021 stimulation, hiPSCs were transferred from hypoxia to normoxia. At day 2 of differentiation, hiPSC-derived mesodermal cells were fed with basal medium supplemented with 4 μM IWR-1 (Merck) for 48 h to induce cardiac progenitor cell differentiation. From day 4 onwards, the medium was changed every other day with CM maintenance medium (RPMI 1640, rice-derived recombinant human albumin, and L-ascorbic acid 2-phosphate). Contracting CMs appeared at day 8 or 9 of cardiac differentiation. DMD hiPSC-CMs were treated with 3 mM NAC and 0.5 μM idebenone from day 8 onwards, and 20 μg/mL ataluren (PTC124) was supplemented to the cardiac differentiation medium from day 4 onwards. In *NOX4* knockdown experiments, 250 nM of single-stranded antisense oligonucleotides for silencing *NOX4* mRNA, called Antisense LNA GapmeRs (Qiagen), were added to the cell cultures at day 8 of differentiation.

Generation of 3D EHT constructs

3D EHT constructs were generated from 8- to 10-day-old hiPSC-CMs, as previously described (Breckwoldt et al., 2017). CMs were dissociated with collagenase A (1 U/mL; Merck) for 20 min at 37°C and transferred to custom-made 2% agarose (UltraPure; Thermo Fisher Scientific) casting molds in 24-well plate formats. The single-cell suspension was maintained in DMEM low glucose medium containing 10% fetal bovine serum (FBS), 1% heat-inactivated horse serum (HS), 1% Pen/Strep (all from Thermo Fisher Scientific), and 0.1% Rho-associated protein kinase (ROCK) inhibitor (Y-27632; VWR). Each EHT construct consisted of 1.0×10^6 cells supplemented with GFR Matrigel, 5.06% fibrinogen (human plasma; Merck), 3U/mL thrombin (Stago BNL), and 1.44% aprotinin (Merck). The casting was performed around two flexible polydimethylsiloxane (PDMS) microposts within the agarose molds. After 2 h of incubation, polymerization formed a fibrin block around the microposts, embedding the single-cell suspension. The fibrin block was removed from the casting molds and transferred to 24-well plates containing an EHT medium composed of DMEM low glucose, 10% heat-inactivated HS, 1% Pen/Strep, 0.1% aprotinin, and 0.1% human insulin solution (Merck). Medium was changed every other day with EHT medium.

SUPPLEMENTAL INFORMATION

Supplemental information can be found online at https://doi.org/10.1016/j.stemcr.2021.12.019.

AUTHOR CONTRIBUTIONS

R.D. participated in conception and design, collection and assembly of data, data analysis and interpretation, and manuscript

writing. D.C. participated in western blot collection and assembly of data, data analysis and interpretation, and reviewed the manuscript. G.G. participated in patch-clamp electrophysiology and Ca^{2+} recordings, data analysis and interpretation, and reviewed the manuscript. L.D.W. provided DMD patient study samples, participated in conception and design, data analysis and interpretation, and reviewed the manuscript. N.G. provided DMD patient study samples and reviewed the manuscript. K.D. participated in data analysis and interpretation and reviewed the manuscript. C.M.V. participated in conception and design, data analysis and interpretation, and reviewed the manuscript. K.R.S. participated in conception and design, data analysis and interpretation, and reviewed the manuscript. G.M.B. and M.S. participated in conception and design, data analysis and interpretation, reviewed the manuscript, and gave final approval for manuscript submission.

CONFLICT OF INTERESTS

G.M.B. was an Investigator for clinical trials in DMD sponsored by Santhera Pharmaceuticals. G.M.B. is a co-inventor of relevant patent applications. The investigators and authors had sole discretion over study design, collection, analysis and interpretation of data, writing of the report, and the decision to submit the manuscript for publication. All other authors declare no competing interests.

ACKNOWLEDGMENTS

The authors thank Santhera Pharmaceuticals (Pratteln, Switzerland) for providing idebenone. The authors gratefully acknowledge Hanne Grosemans and Sylvia Sauvage for technical assistance; Ewa Berlińska, Filippo Conti, Vittoria Marini, and Ilaria Tortorella for assistance during their internship period at the KU Leuven; and Christina Vochten and Vicky Raets for the administrative assistance. R.D. is supported by KU Leuven Rondoufonds voor Duchenne Onderzoek (EQQ-FODUCH-O2010) and an internal KU Leuven grant (C24/18/103). This work has been supported with the contributions of INTERREG – Euregio Meuse-Rhine (GYM – Generate your muscle 2020-EMR116), FWO (#G066821N) and KU Leuven C1-3DMuSyC (C14/17/111) grants. G.M.B. is Senior Clinical Investigator of the Research Foundation Flanders (FWO Vlaanderen, Belgium).

Received: December 10, 2021
Revised: December 22, 2021
Accepted: December 26, 2021
Published: January 27, 2022

REFERENCES

Ago, T., Kuroda, J., Pain, J., Fu, C., Li, H., and Sadoshima, J. (2010). Upregulation of Nox4 by hypertrophic stimuli promotes apoptosis and mitochondrial dysfunction in cardiac myocytes. Circ. Res. *106*, 1253–1264. https://doi.org/10.1161/CIRCRESAHA.109.213116.

Allen, D.G., Whitehead, N.P., and Froehner, S.C. (2016). Absence of dystrophin disrupts skeletal muscle signaling: roles of Ca2+, reactive oxygen species, and nitric oxide in the development of muscular dystrophy. Physiol. Rev. *96*, 253–305. https://doi.org/10.1152/physrev.00007.2015.

Atmanli, A., Chai, A.C., Cui, M., Wang, Z., Nishiyama, T., Bassel-Duby, R., and Olson, E.N. (2021). Cardiac myoediting attenuates cardiac abnormalities in human and mouse models of duchenne muscular dystrophy. Circ. Res. https://doi.org/10.1161/CIRCRESAHA.121.319579.

Bajek, A., Porowinska, D., Kloskowski, T., Brzoska, E., Ciemerych, M.A., and Drewa, T. (2015). Cell therapy in Duchenne muscular dystrophy treatment: clinical trials overview. Crit. Rev. Eukaryot. Gene Expr. *25*, 1–11. https://doi.org/10.1615/critreveukaryotgeneexpr.2015011074.

Bartsch, C., Bekhite, M.M., Wolheim, A., Richter, M., Ruhe, C., Wissuwa, B., Marciniak, A., Muller, J., Heller, R., Figulla, H.R., et al. (2011). NADPH oxidase and eNOS control cardiomyogenesis in mouse embryonic stem cells on ascorbic acid treatment. Free Radic. Biol. Med. *51*, 432–443. https://doi.org/10.1016/j.freeradbiomed.2011.04.029.

Belmokhtar, C.A., Hillion, J., and Segal-Bendirdjian, E. (2001). Staurosporine induces apoptosis through both caspase-dependent and caspase-independent mechanisms. Oncogene *20*, 3354–3362. https://doi.org/10.1038/sj.onc.1204436.

Breckwoldt, K., Letuffe-Breniere, D., Mannhardt, I., Schulze, T., Ulmer, B., Werner, T., Benzin, A., Klampe, B., Reinsch, M.C., Laufer, S., et al. (2017). Differentiation of cardiomyocytes and generation of human engineered heart tissue. Nat. Protoc. *12*, 1177–1197. https://doi.org/10.1038/nprot.2017.033.

Burridge, P.W., Matsa, E., Shukla, P., Lin, Z.C., Churko, J.M., Ebert, A.D., Lan, F., Diecke, S., Huber, B., Mordwinkin, N.M., et al. (2014). Chemically defined generation of human cardiomyocytes. Nat. Methods *11*, 855–860. https://doi.org/10.1038/nmeth.2999.

Buyse, G.M., Voit, T., Schara, U., Straathof, C.S.M., D'Angelo, M.G., Bernert, G., Cuisset, J.M., Finkel, R.S., Goemans, N., McDonald, C.M., et al. (2015). Efficacy of idebenone on respiratory function in patients with Duchenne muscular dystrophy not using glucocorticoids (DELOS): a double-blind randomised placebo-controlled phase 3 trial. Lancet *385*, 1748–1757. https://doi.org/10.1016/S0140-6736(15)60025-3.

Calos, M.P. (2016). The CRISPR way to think about Duchenne's. N. Engl. J. Med. *374*, 1684–1686. https://doi.org/10.1056/NEJMcibr1601383.

Campbell, C., Barohn, R.J., Bertini, E., Chabrol, B., Comi, G.P., Darras, B.T., Finkel, R.S., Flanigan, K.M., Goemans, N., Iannaccone, S.T., et al. (2020). Meta-analyses of ataluren randomized controlled trials in nonsense mutation Duchenne muscular dystrophy. J. Comp. Eff. Res. https://doi.org/10.2217/cer-2020-0095.

Cao, N., Liu, Z., Chen, Z., Wang, J., Chen, T., Zhao, X., Ma, Y., Qin, L., Kang, J., Wei, B., et al. (2012). Ascorbic acid enhances the cardiac differentiation of induced pluripotent stem cells through promoting the proliferation of cardiac progenitor cells. Cell Res. *22*, 219–236. https://doi.org/10.1038/cr.2011.195.

Davies, K.E., and Nowak, K.J. (2006). Molecular mechanisms of muscular dystrophies: old and new players. Nat. Rev. Mol. Cell Biol. *7*, 762–773. https://doi.org/10.1038/nrm2024.

Eisen, B., Ben Jehuda, R., Cuttitta, A.J., Mekies, L.N., Shemer, Y., Baskin, P., Reiter, I., Willi, L., Freimark, D., Gherghiceanu, M., et al. (2019). Electrophysiological abnormalities in induced

pluripotent stem cell-derived cardiomyocytes generated from Duchenne muscular dystrophy patients. J. Cell Mol. Med. *23*, 2125–2135. https://doi.org/10.1111/jcmm.14124.

Emery, A.E. (2002). The muscular dystrophies. Lancet *359*, 687–695. https://doi.org/10.1016/S0140-6736(02)07815-7.

Fukumura, H., Sato, M., Kezuka, K., Sato, I., Feng, X., Okumura, S., Fujita, T., Yokoyama, U., Eguchi, H., Ishikawa, Y., and Saito, T. (2012). Effect of ascorbic acid on reactive oxygen species production in chemotherapy and hyperthermia in prostate cancer cells. J. Physiol. Sci. *62*, 251–257. https://doi.org/10.1007/s12576-012-0204-0.

Kerr, J.P., Robison, P., Shi, G., Bogush, A.I., Kempema, A.M., Hexum, J.K., Becerra, N., Harki, D.A., Martin, S.S., Raiteri, R., et al. (2015). Detyrosinated microtubules modulate mechanotransduction in heart and skeletal muscle. Nat. Commun. *6*, 8526. https://doi.org/10.1038/ncomms9526.

Khairallah, R.J., Shi, G., Sbrana, F., Prosser, B.L., Borroto, C., Mazaitis, M.J., Hoffman, E.P., Mahurkar, A., Sachs, F., Sun, Y., et al. (2012). Microtubules underlie dysfunction in duchenne muscular dystrophy. Sci. Signal. *5*, ra56. https://doi.org/10.1126/scisignal.2002829.

Kolwicz, S.C., Jr., Odom, G.L., Nowakowski, S.G., Moussavi-Harami, F., Chen, X., Reinecke, H., Hauschka, S.D., Murry, C.E., Mahairas, G.G., and Regnier, M. (2016). AAV6-mediated cardiac-specific overexpression of ribonucleotide reductase enhances myocardial contractility. Mol. Ther. *24*, 240–250. https://doi.org/10.1038/mt.2015.176.

Kyrychenko, V., Kyrychenko, S., Tiburcy, M., Shelton, J.M., Long, C., Schneider, J.W., Zimmermann, W.H., Bassel-Duby, R., and Olson, E.N. (2017). Functional correction of dystrophin actin binding domain mutations by genome editing. JCI Insight *2*. https://doi.org/10.1172/jci.insight.95918.

Landfeldt, E., Thompson, R., Sejersen, T., McMillan, H.J., Kirschner, J., and Lochmuller, H. (2020). Life expectancy at birth in Duchenne muscular dystrophy: a systematic review and meta-analysis. Eur. J. Epidemiol. *35*, 643–653. https://doi.org/10.1007/s10654-020-00613-8.

Lin, B., Li, Y., Han, L., Kaplan, A.D., Ao, Y., Kalra, S., Bett, G.C., Rasmusson, R.L., Denning, C., and Yang, L. (2015). Modeling and study of the mechanism of dilated cardiomyopathy using induced pluripotent stem cells derived from individuals with Duchenne muscular dystrophy. Dis. Model. Mech. *8*, 457–466. https://doi.org/10.1242/dmm.019505.

Mathur, A., Hong, Y., Kemp, B.K., Barrientos, A.A., and Erusalimsky, J.D. (2000). Evaluation of fluorescent dyes for the detection of mitochondrial membrane potential changes in cultured cardiomyocytes. Cardiovasc. Res. *46*, 126–138. https://doi.org/10.1016/s0008-6363(00)00002-x.

Mercuri, E., Bonnemann, C.G., and Muntoni, F. (2019). Muscular dystrophies. Lancet *394*, 2025–2038. https://doi.org/10.1016/S0140-6736(19)32910-1.

Moretti, A., Fonteyne, L., Giesert, F., Hoppmann, P., Meier, A.B., Bozoglu, T., Baehr, A., Schneider, C.M., Sinnecker, D., Klett, K., et al. (2020). Somatic gene editing ameliorates skeletal and cardiac muscle failure in pig and human models of Duchenne muscular dystrophy. Nat. Med. *26*, 207–214. https://doi.org/10.1038/s41591-019-0738-2.

Moussavi-Harami, F., Razumova, M.V., Racca, A.W., Cheng, Y., Stempien-Otero, A., and Regnier, M. (2015). 2-Deoxy adenosine triphosphate improves contraction in human end-stage heart failure. J. Mol. Cell Cardiol. *79*, 256–263. https://doi.org/10.1016/j.yjmcc.2014.12.002.

Mummery, C.L., Zhang, J., Ng, E.S., Elliott, D.A., Elefanty, A.G., and Kamp, T.J. (2012). Differentiation of human embryonic stem cells and induced pluripotent stem cells to cardiomyocytes: a methods overview. Circ. Res. *111*, 344–358. https://doi.org/10.1161/CIRCRESAHA.110.227512.

Pioner, J.M., Guan, X., Klaiman, J.M., Racca, A.W., Pabon, L., Muskheli, V., Macadangdang, J., Ferrantini, C., Hoopmann, M.R., Moritz, R.L., et al. (2020). Absence of full-length dystrophin impairs normal maturation and contraction of cardiomyocytes derived from human-induced pluripotent stem cells. Cardiovasc. Res. *116*, 368–382. https://doi.org/10.1093/cvr/cvz109.

Prosser, B.L., Ward, C.W., and Lederer, W.J. (2011). X-ROS signaling: rapid mechano-chemo transduction in heart. Science *333*, 1440–1445. https://doi.org/10.1126/science.1202768.

Sato, M., Shiba, N., Miyazaki, D., Shiba, Y., Echigoya, Y., Yokota, T., Takizawa, H., Aoki, Y., Takeda, S., and Nakamura, A. (2019). Amelioration of intracellular Ca(2+) regulation by exon-45 skipping in Duchenne muscular dystrophy-induced pluripotent stem cell-derived cardiomyocytes. Biochem. Biophys. Res. Commun. *520*, 179–185. https://doi.org/10.1016/j.bbrc.2019.09.095.

Sesso, H.D., Buring, J.E., Christen, W.G., Kurth, T., Belanger, C., MacFadyen, J., Bubes, V., Manson, J.E., Glynn, R.J., and Gaziano, J.M. (2008). Vitamins E and C in the prevention of cardiovascular disease in men: the Physicians' Health Study II randomized controlled trial. JAMA *300*, 2123–2133. https://doi.org/10.1001/jama.2008.600.

Shanmugasundaram, K., Nayak, B.K., Friedrichs, W.E., Kaushik, D., Rodriguez, R., and Block, K. (2017). NOX4 functions as a mitochondrial energetic sensor coupling cancer metabolic reprogramming to drug resistance. Nat. Commun. *8*, 997. https://doi.org/10.1038/s41467-017-01106-1.

Spurney, C.F., Knoblach, S., Pistilli, E.E., Nagaraju, K., Martin, G.R., and Hoffman, E.P. (2008). Dystrophin-deficient cardiomyopathy in mouse: expression of Nox4 and Lox are associated with fibrosis and altered functional parameters in the heart. Neuromuscul. Disord. *18*, 371–381. https://doi.org/10.1016/j.nmd.2008.03.008.

Takahashi, K., and Yamanaka, S. (2006). Induction of pluripotent stem cells from mouse embryonic and adult fibroblast cultures by defined factors. Cell *126*, 663–676. https://doi.org/10.1016/j.cell.2006.07.024.

Timpani, C.A., Hayes, A., and Rybalka, E. (2015). Revisiting the dystrophin-ATP connection: how half a century of research still implicates mitochondrial dysfunction in Duchenne muscular dystrophy aetiology. Med. Hypotheses *85*, 1021–1033. https://doi.org/10.1016/j.mehy.2015.08.015.

Varga, Z.V., Pipicz, M., Baan, J.A., Baranyai, T., Koncsos, G., Leszek, P., Kusmierczyk, M., Sanchez-Cabo, F., Garcia-Pavia, P., Brenner, G.J., et al. (2017). Alternative splicing of NOX4 in the failing

human heart. Front. Physiol. *8*, 935. https://doi.org/10.3389/fphys.2017.00935.

Verhaart, I.E.C., and Aartsma-Rus, A. (2019). Therapeutic developments for Duchenne muscular dystrophy. Nat. Rev. Neurol. *15*, 373–386. https://doi.org/10.1038/s41582-019-0203-3.

Vermot, A., Petit-Hartlein, I., Smith, S.M.E., and Fieschi, F. (2021). NADPH oxidases (NOX): an overview from discovery, molecular mechanisms to physiology and pathology. Antioxidants *10*. https://doi.org/10.3390/antiox10060890.

Walker, J.E., Saraste, M., Runswick, M.J., and Gay, N.J. (1982). Distantly related sequences in the alpha- and beta-subunits of ATP synthase, myosin, kinases and other ATP-requiring enzymes and a common nucleotide binding fold. EMBO J. *1*, 945–951.

Wei, X., Xu, Y., Xu, F.F., Chaiswing, L., Schnell, D., Noel, T., Wang, C., Chen, J., St Clair, D.K., and St Clair, W.H. (2017). RelB expression determines the differential effects of ascorbic acid in normal and cancer cells. Cancer Res. *77*, 1345–1356. https://doi.org/10.1158/0008-5472.CAN-16-0785.

Welch, E.M., Barton, E.R., Zhuo, J., Tomizawa, Y., Friesen, W.J., Trifillis, P., Paushkin, S., Patel, M., Trotta, C.R., Hwang, S., et al. (2007). PTC124 targets genetic disorders caused by nonsense mutations. Nature *447*, 87–91. https://doi.org/10.1038/nature05756.

Wu, B., Moulton, H.M., Iversen, P.L., Jiang, J., Li, J., Li, J., Spurney, C.F., Sali, A., Guerron, A.D., Nagaraju, K., et al. (2008). Effective rescue of dystrophin improves cardiac function in dystrophin-deficient mice by a modified morpholino oligomer. Proc. Natl. Acad. Sci. U S A *105*, 14814–14819. https://doi.org/10.1073/pnas.0805676105.

Zhang, M., Perino, A., Ghigo, A., Hirsch, E., and Shah, A.M. (2013). NADPH oxidases in heart failure: poachers or gamekeepers? Antioxid. Redox Signal. *18*, 1024–1041. https://doi.org/10.1089/ars.2012.4550.

Zorova, L.D., Popkov, V.A., Plotnikov, E.Y., Silachev, D.N., Pevzner, I.B., Jankauskas, S.S., Babenko, V.A., Zorov, S.D., Balakireva, A.V., Juhaszova, M., et al. (2018). Mitochondrial membrane potential. Anal. Biochem. *552*, 50–59. https://doi.org/10.1016/j.ab.2017.07.009.

Stem Cell Reports, Volume *17*

Supplemental Information

Human iPSC model reveals a central role for NOX4 and oxidative stress in Duchenne cardiomyopathy

Robin Duelen, Domiziana Costamagna, Guillaume Gilbert, Liesbeth De Waele, Nathalie Goemans, Kaat Desloovere, Catherine M. Verfaillie, Karin R. Sipido, Gunnar M. Buyse, and Maurilio Sampaolesi

SUPPLEMENTAL INFORMATION (Duelen et al.)

SUPPLEMENTAL ITEMS (FIGURES AND TABLES)

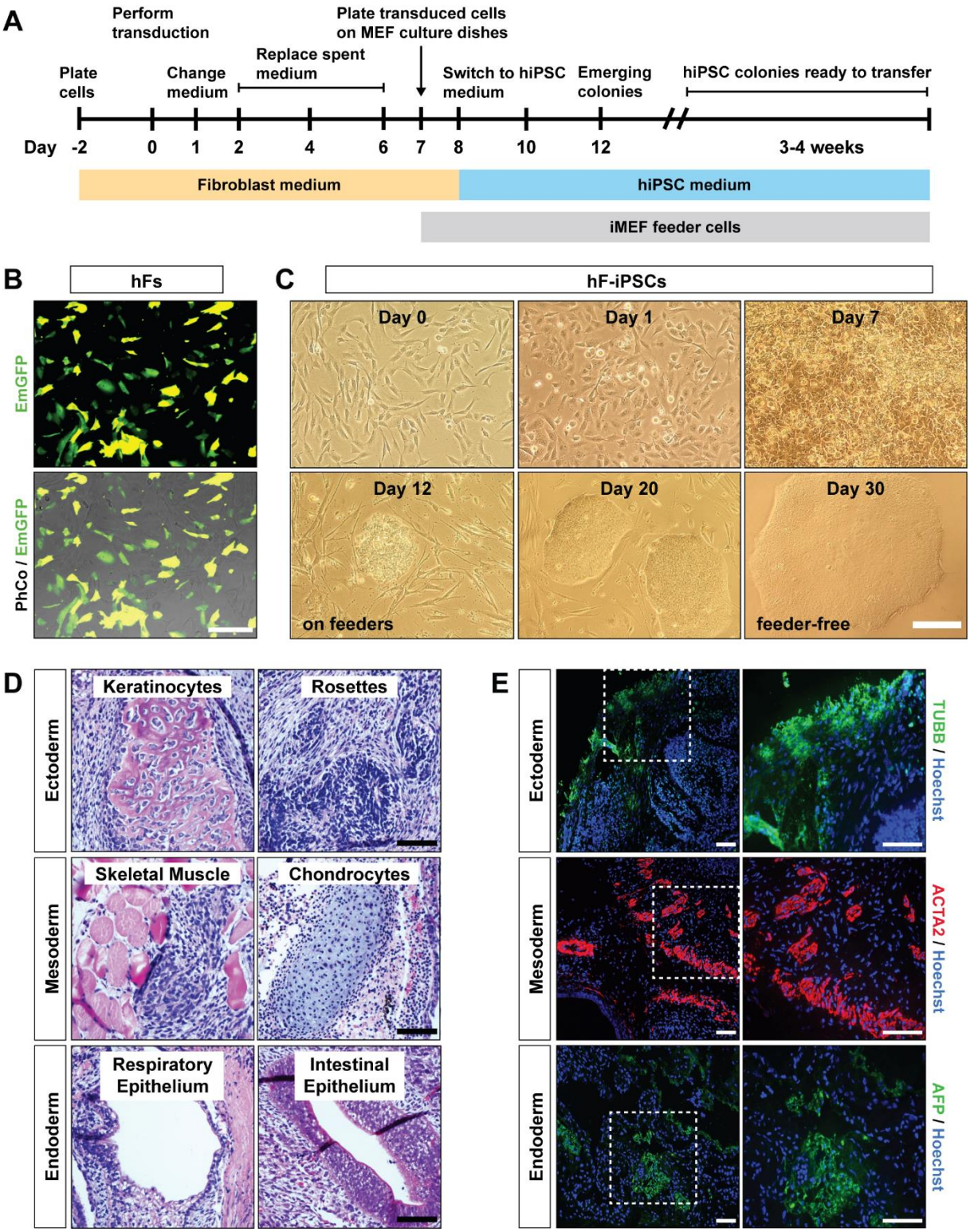

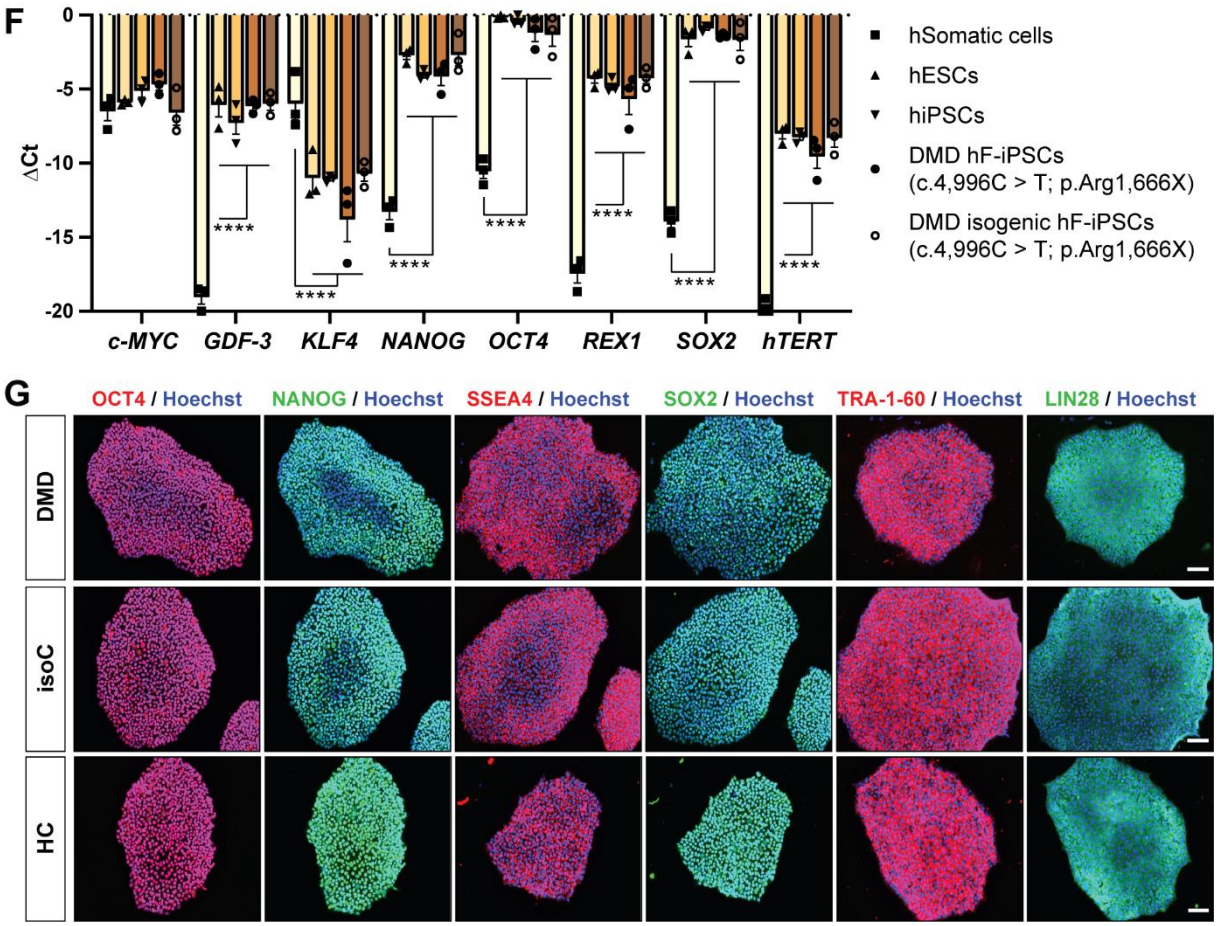

Fig. S1: Characterization of the SeV-mediated reprogrammed DMD patient hF-iPSC clones, harboring the nonsense mutation in exon 35 (c.4,996C > T; p.Arg1,666X) of the *Dystrophin* gene, and its CRISPR-Cas9 corrected DMD isogenic control line. (A) Schematic representation of the SeV hiPSC reprogramming protocol for hFs (data not shown for hPBMCs). hFs were transduced at day 0 using the integration-free SeV vectors, expressing the OSKM (OCT3/4, SOX2, KLF4 and c-MYC) pluripotency markers. **(B)** EmGFP (green) expression of transduced DMD somatic cells, 1 day after transduction with SeV reprogramming vectors. **(C)** Morphological progression of DMD hFs towards hiPSC clones. **(D)** Hematoxylin and eosin staining on SeV-reprogrammed hiPSC-induced *in vivo* teratomas showing the derivatives of the three developmental germ layers, including keratinocytes and rosettes (ectoderm), skeletal muscle fibers and chondrocytes (mesoderm), and epithelium from respiratory and intestinal tract (endoderm). **(E)** Immunostaining of three germ lineage markers: Beta Tubulin (TUBB; ectoderm), Alpha Smooth Muscle Actin (ACTA2; mesoderm) and Alpha Fetoprotein (AFP; endoderm). Scale bar = 100 μm. The pluripotency state of the DMD isogenic control line. The following pluripotency genes (*c-MYC, GDF-3, KLF4, NANOG, OCT4, REX1, SOX2* and *hTERT*) **(F)** and proteins (OCT4, NANOG, SSEA4, SOX2, TRA-1-60 and LIN28) **(G)** were analyzed. Human embryonic stem cell lines (hESCs) and commercially available undifferentiated hiPSC lines were used as positive controls. Each data point was represented as ΔCt, normalized for the housekeeping genes (*GAPDH, HPRT* and *RPL13a*). Data were representative of three independent experiments (n = 3) and values were expressed as mean ± SEM. Significance of the difference was indicated as follows: *p < 0.05; **p < 0.01; ***p < 0.001 and ****p < 0.0001. Scale bar = 100 μm.

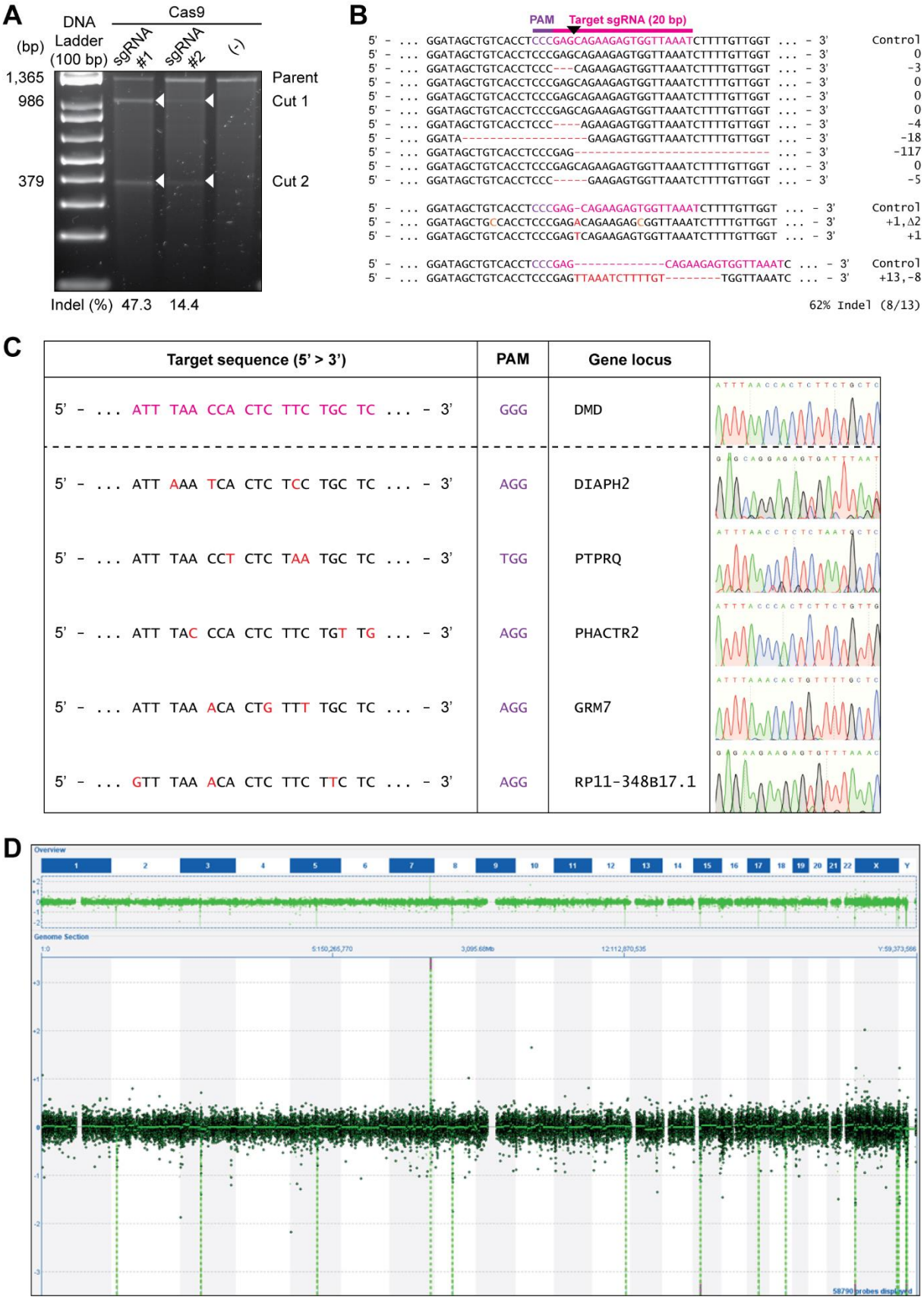

Fig. S2: Validation of the Cas9 cutting efficiency and analysis of the off-targets. (A) Surveyor assay in HEK293T cells to evaluate the cutting efficiency of the sgRNAs, represented as random events of base pair (bp) insertions or deletions (indel) after DSB. **(B)** DNA sequencing of the NHEJ events after transfection of the sgRNA-Cas9 plasmids in HEK293T cells. **(C)** List of CRISPR-Cas9 off-targets

(source: www.synthego.com). **(D)** Detailed CGH molecular karyotyping showing no additional chromosomal abnormalities due to unwanted Cas9-mediated DSB cuts.

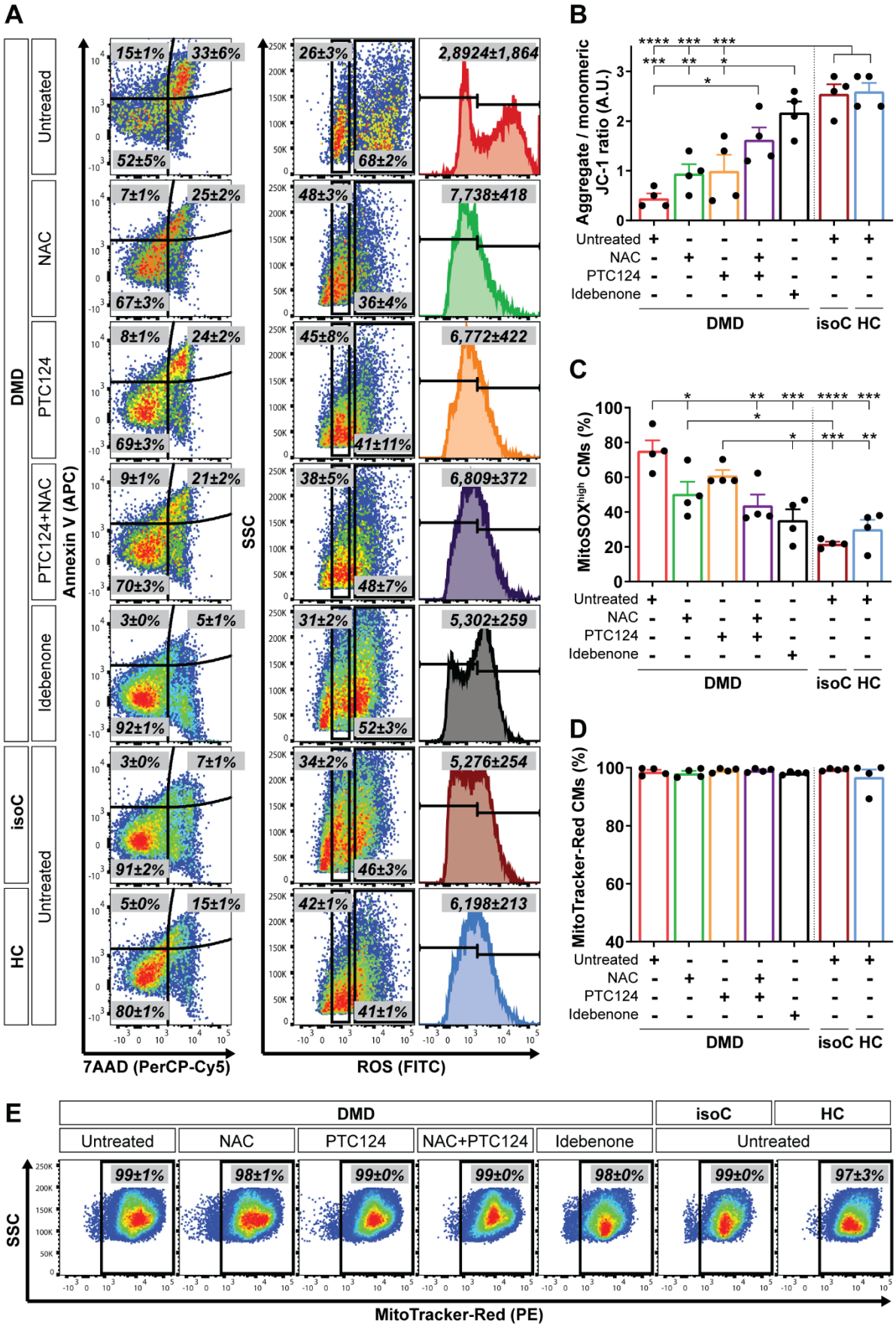

Fig. S3: Corresponding flow cytometric graphs and quantification for the characterization of the cardiomyopathic phenotype of DMD hiPSC-CMs, showing premature cell death, depolarized

mitochondria and increased intracellular ROS levels. (A) Representative flow cytometric analyses at day 15 of cardiac differentiation showing the percentage of cell death (using annexin V, APC and 7AAD, PerCP-Cy5, *left panels*) and intracellular ROS (FITC, *right panels*) in untreated and treated DMD hiPSC-CMs compared to the DMD isogenic and healthy controls. Human iPSC-CMs were stained for SIRPA (PE) to obtain high CM purity (data not shown). Flow cytometric quantification at day 15 of differentiation showing the JC-1 aggregates/monomers ratio **(B)** and the mitochondrial superoxide production (MitoSOX) in depolarized DMD mitochondria **(C)** compared to DMD isogenic and healthy controls. **(D)** Percentage of MitoTracker-Red positive CMs upon NAC, PTC124 and idebenone treatment. **(E)** Corresponding flow cytometric analyses of the percentage of MitoTracker-Red (PE) positive hiPSC-CMs. Data were representative of four independent experiments (n = 4). Data were reported as mean ± SEM; *p < 0.05; **p < 0.01; ***p < 0.001 and ****p < 0.0001.

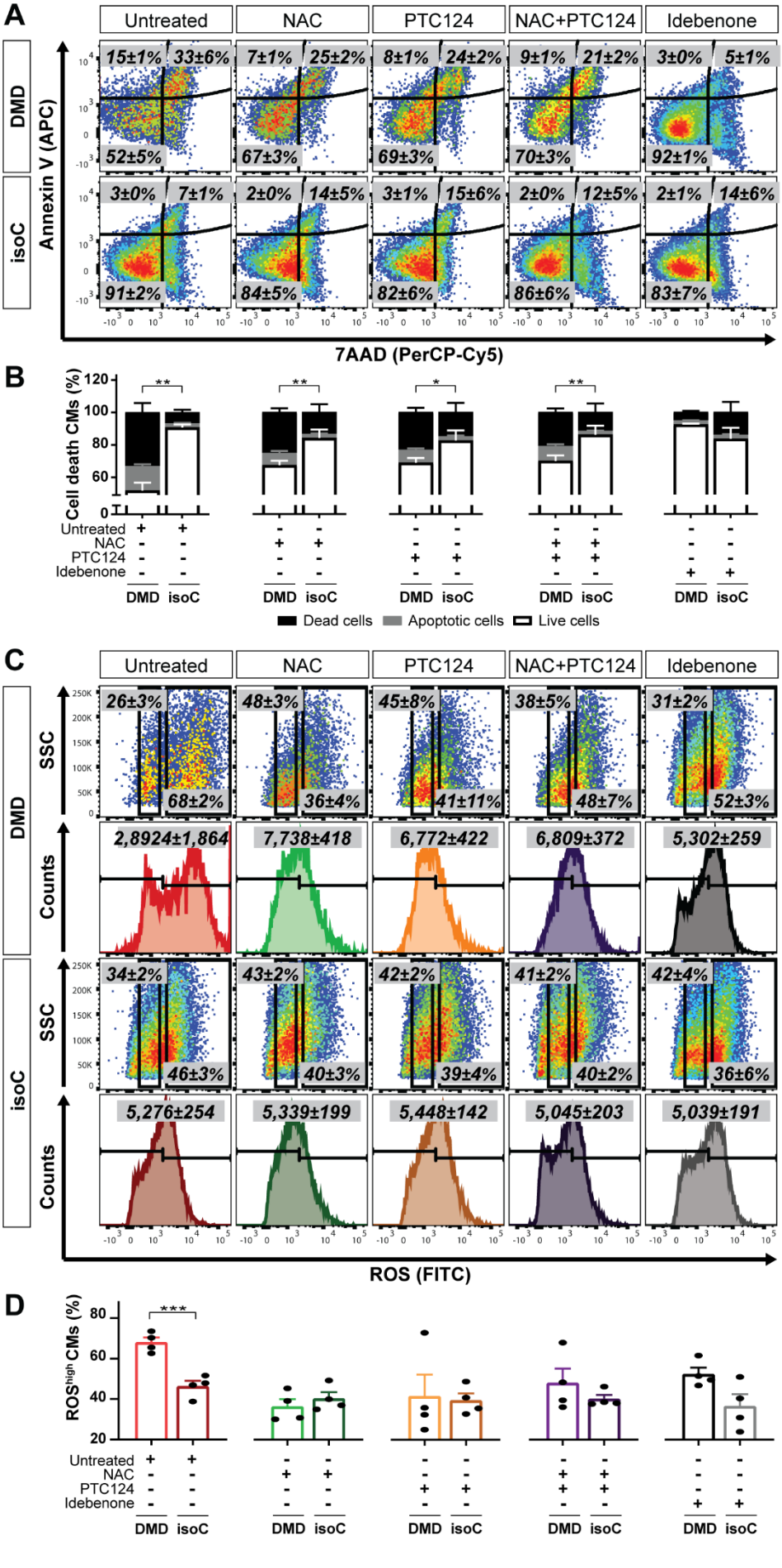
A
Untreated
NAC
PTC124
NAC+PTC124
Idebenone
DMD
isoC
Annexin V (APC)
7AAD (PerCP-Cy5)
15±1%
33±6%
7±1%
25±2%
8±1%
24±2%
9±1%
21±2%
3±0%
5±1%
52±5%
67±3%
69±3%
70±3%
92±1%
3±0%
7±1%
2±0%
14±5%
3±1%
15±6%
2±0%
12±5%
2±1%
14±6%
91±2%
84±5%
82±6%
86±6%
83±7%
B
Cell death CMs (%)
Untreated
NAC
PTC124
Idebenone
DMD
isoC
Dead cells
Apoptotic cells
Live cells
C
SSC
Counts
ROS (FITC)
26±3%
48±3%
45±8%
38±5%
31±2%
68±2%
36±4%
41±11%
48±7%
52±3%
2,8924±1,864
7,738±418
6,772±422
6,809±372
5,302±259
34±2%
43±2%
42±2%
41±2%
42±4%
46±3%
40±3%
39±4%
40±2%
36±6%
5,276±254
5,339±199
5,448±142
5,045±203
5,039±191
D
ROS^high CMs (%)

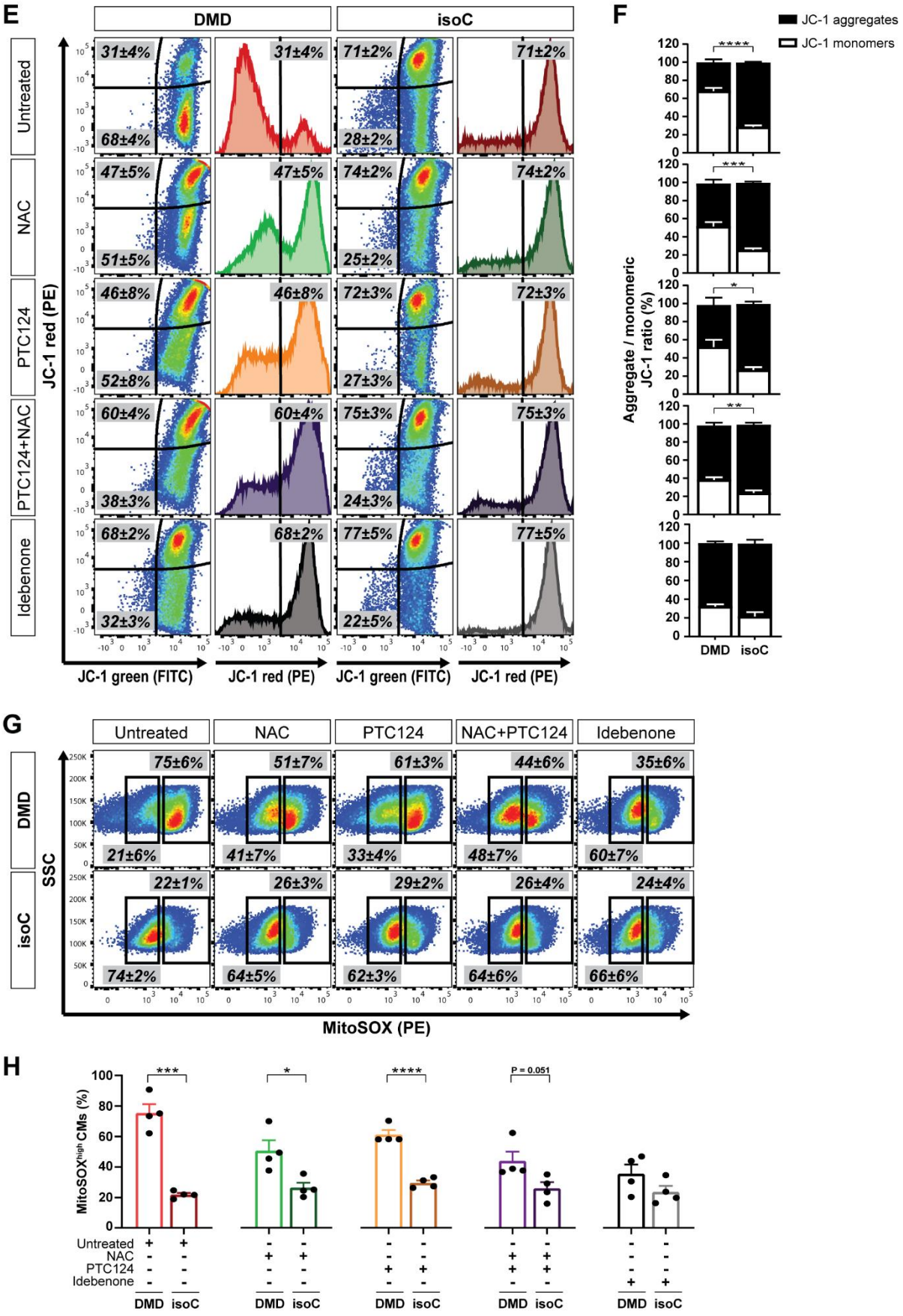
E
DMD
isoC
Untreated
NAC
PTC124
PTC124+NAC
Idebenone
JC-1 red (PE)
JC-1 green (FITC)
JC-1 red (PE)
JC-1 green (FITC)
JC-1 red (PE)
31±4%
68±4%
31±4%
71±2%
28±2%
71±2%
47±5%
51±5%
47±5%
74±2%
25±2%
74±2%
46±8%
52±8%
46±8%
72±3%
27±3%
72±3%
60±4%
38±3%
60±4%
75±3%
24±3%
75±3%
68±2%
32±3%
68±2%
77±5%
22±5%
77±5%
F
JC-1 aggregates
JC-1 monomers
Aggregate / monomeric JC-1 ratio (%)
****
***
*
**
DMD
isoC
G
Untreated
NAC
PTC124
NAC+PTC124
Idebenone
DMD
isoC
SSC
MitoSOX (PE)
75±6%
21±6%
51±7%
41±7%
61±3%
33±4%
44±6%
48±7%
35±6%
60±7%
22±1%
74±2%
26±3%
64±5%
29±2%
62±3%
26±4%
64±6%
24±4%
66±6%
H
MitoSOXhigh CMs (%)
***
*
****
P = 0.051
Untreated
NAC
PTC124
Idebenone
DMD
isoC

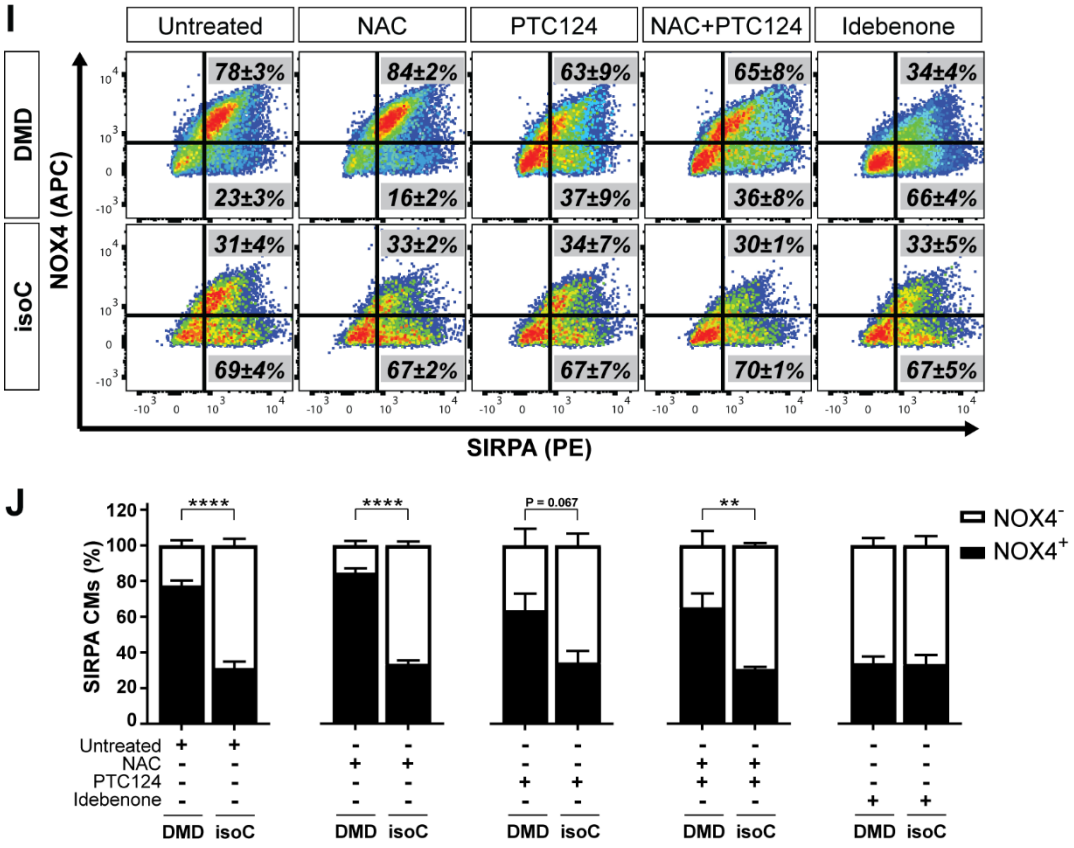

Fig. S4: Specificity of the treatment options on cell death and intracellular ROS concentrations, on $\Delta\Psi_m$ and mitochondrial superoxide concentrations, and on the expression levels of NOX4 in the experimental hiPSC-CM groups. (A) Example of flow cytometric analysis at day 15 of cardiac differentiation showing the percentage of cell death (using annexin V, APC and 7AAD, PerCP-Cy5) upon treatment in SIRPA (PE) positive hiPSC-CMs derived from DMD and DMD isogenic controls. **(B)** Corresponding flow cytometric quantification for cell death observed after the treatment options. **(C)** Representative flow cytometric analyses showing intracellular ROS concentrations in DMD and DMD isogenic hiPSC-CMs. **(D)** Quantification of the corresponding flow cytometric analyses showing the intracellular ROS levels. Data were representative of four independent experiments (n = 4). Data were reported as mean ± SEM; *p < 0.05; **p < 0.01; ***p < 0.001 and ****p < 0.0001. **(E)** Representative flow cytometric analyses at day 15 of cardiac differentiation for JC-1 aggregates (PE) and JC-1 monomers (FITC) upon treatment in DMD hiPSC-CMs and the DMD isogenic counterpart. **(F)** Corresponding flow cytometric quantification for $\Delta\Psi_m$. **(G)** Flow cytometric analyses at day 15 of differentiation showing the mitochondrial superoxide production (MitoSOX, PE) in depolarized DMD mitochondria. **(H)** Quantification of the corresponding flow cytometric analyses showing the mitochondrial superoxide production (MitoSOX). Data were representative of four independent experiments (n = 4). Flow cytometry data were reported as mean ± SEM; *p < 0.05; **p < 0.01; ***p < 0.001 and ****p < 0.0001. **(I)** Example of flow cytometric analysis at day 15 of cardiac differentiation showing the percentage of NOX4 (APC) on SIRPA (PE) positive DMD and DMD isogenic hiPSC-CMs upon the treatment options. **(J)** Corresponding flow cytometric quantification for NOX4. Data were representative of three independent experiments (n = 3). Flow cytometry data were reported as mean ± SEM; *p < 0.05; **p < 0.01; ***p < 0.001 and ****p < 0.0001.

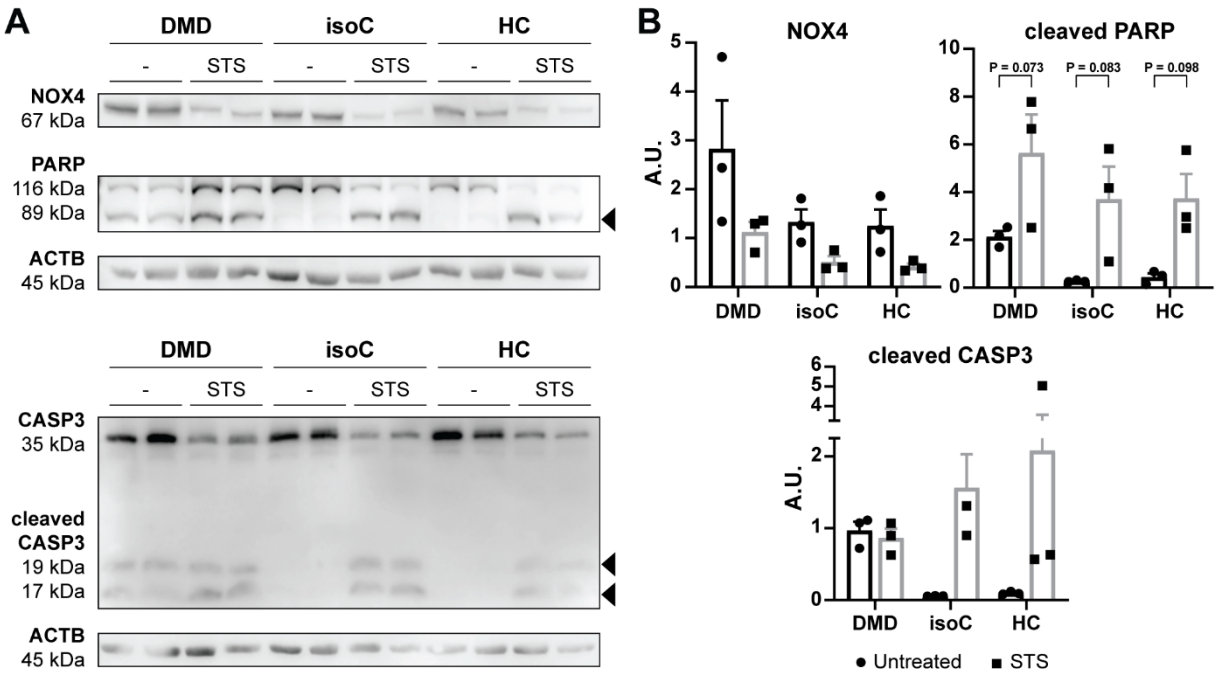

Fig. S5: NOX4 protein expression levels after STS-induced cell death in DMD and control hiPSC-CMs. (A) Western blot analysis showing cardiac NOX4 proteins and the cell death markers Poly (ADP-ribose) polymerase (PARP) and Caspase-3 (CASP3) in DMD and control hiPSC-CMs after a 6 h exposure to 1 μM STS. Cleaved forms of PARP and CASP3 are indicated by black triangles. ACTB was used as loading control. **(B)** Quantification of the western blot analysis for the markers NOX4, cleaved PARP and cleaved CASP3. Data were representative of three independent experiments (n = 3) and values were expressed as mean ± SEM.

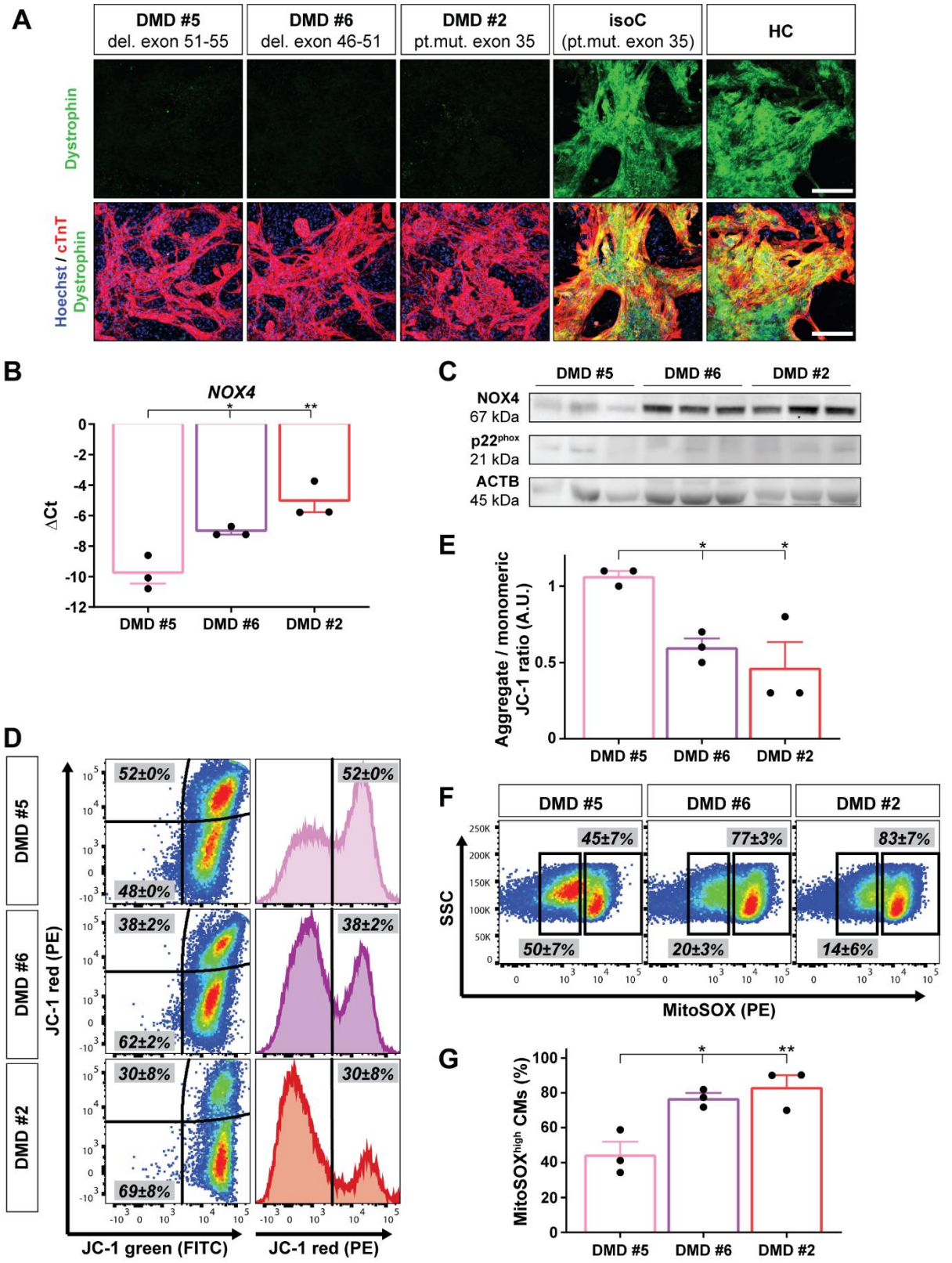

Fig. S6: Characterization of the DMD patient-specific hiPSC-CMs *in vitro*, showing increased NOX4 gene and protein expression levels, depolarized mitochondria and increased intracellular ROS levels. (A) Immunostaining showing the Dystrophin protein expression levels (green) in cTnT positive hiPSC-CMs (cTnT, red and Hoechst, blue), derived from three DMD patient subjects (DMD #2: pt. mut. exon 35; DMD #5: del. exon 51-55 and DMD #6: del. exon 46-51) and controls (see also Table S1). Scale bar = 100 μm. **(B)** *NOX4* mRNA levels in hiPSC-CMs of three DMD patients at day 8 of cardiac differentiation. Each data point was represented as ΔCt, normalized for the housekeeping genes

(*GAPDH* and *RPL13a*). Data were representative of three independent experiments (n = 3) and values were expressed as mean ± SEM; *p < 0.05; **p < 0.01; ***p < 0.001 and ****p < 0.0001. **(C)** Western blot analysis quantifying the corresponding NOX4 protein levels and its regulatory subunit $p22^{phox}$, normalized to the loading protein ACTB. **(D)** Representative flow cytometric analyses at day 15 of differentiation for JC-1 aggregates (PE) and JC-1 monomers (FITC) in three DMD patient-specific hiPSC-CMs. **(E)** Corresponding flow cytometric quantification of JC-1 aggregates and JC-1 monomers. **(F)** Flow cytometric analyses at day 15 of differentiation showing the mitochondrial superoxide production (MitoSOX, PE) in depolarized DMD mitochondria. **(G)** Corresponding flow cytometric quantification for the number of CMs with high mitochondrial superoxide concentrations. Data were representative of three independent experiments (n = 3). Flow cytometry data were reported as mean ± SEM; *p < 0.05; **p < 0.01; ***p < 0.001 and ****p < 0.0001.

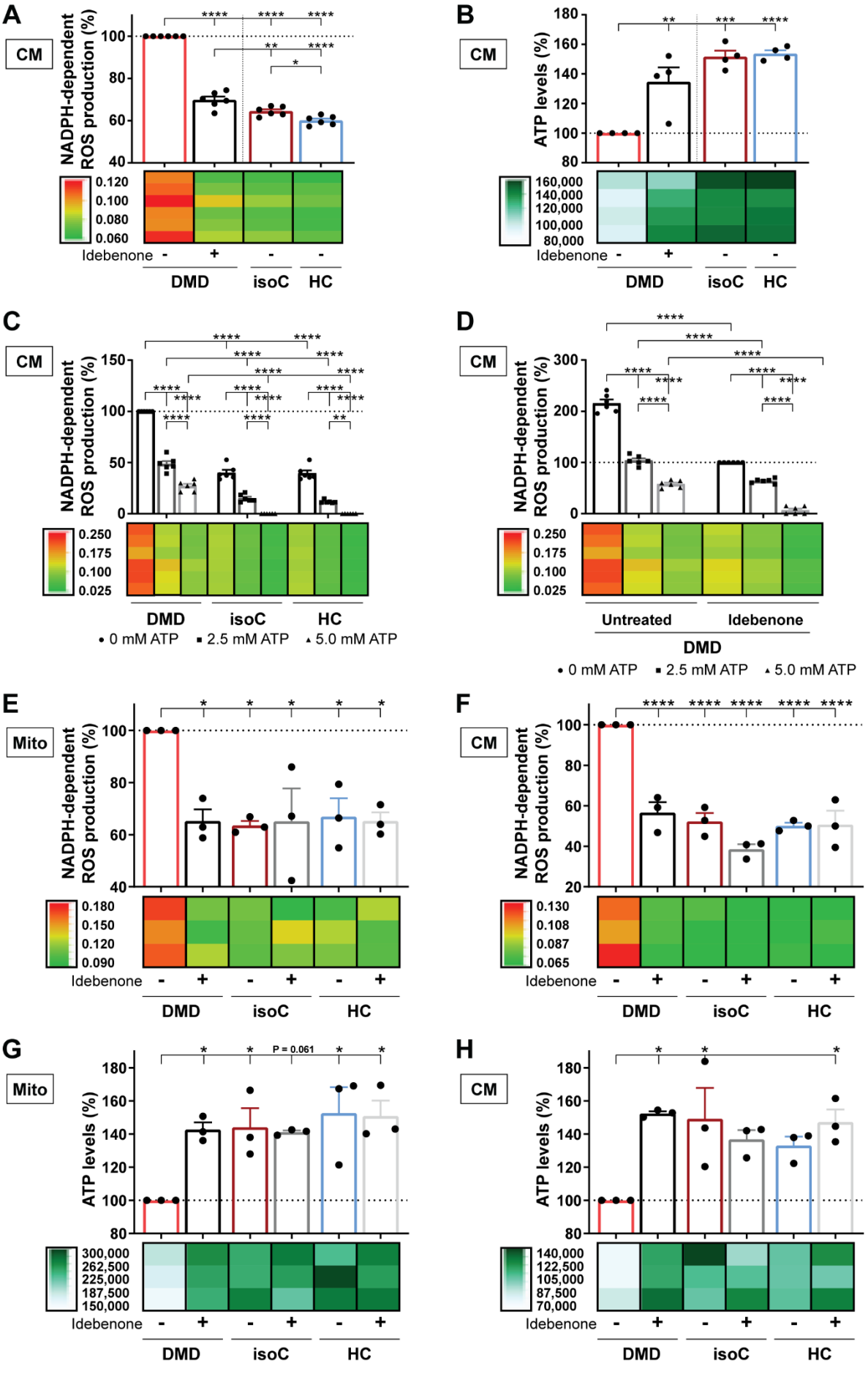
A
CM
NADPH-dependent ROS production (%)
Idebenone
DMD
isoC
HC
B
CM
ATP levels (%)
C
CM
NADPH-dependent ROS production (%)
DMD
isoC
HC
• 0 mM ATP ▪ 2.5 mM ATP ▲ 5.0 mM ATP
D
CM
NADPH-dependent ROS production (%)
Untreated
Idebenone
DMD
• 0 mM ATP ▪ 2.5 mM ATP ▲ 5.0 mM ATP
E
Mito
NADPH-dependent ROS production (%)
F
CM
NADPH-dependent ROS production (%)
G
Mito
ATP levels (%)
P = 0.061
H
CM
ATP levels (%)

Fig. S7: NADPH-dependent ROS production and intracellular ATP levels in DMD hiPSC-CMs after idebenone application, and the specificity of idebenone on the NADPH-dependent ROS production and ATP levels in the experimental hiPSC-CM groups. (A) Quantification of the NADPH-dependent superoxide production of NOX4 in the total CM fraction of DMD hiPSC-CMs with or without idebenone addition compared to controls. **(B)** ATP luminescence detection showing the effect of idebenone treatment on the intracellular ATP levels in DMD hiPSC-CMs. **(C)** Quantification of the ROS-producing NOX4 activity after 2.5 and 5.0 mM ATP addition in DMD hiPSC-CM and control cultures. Each data point was represented as percentage (%), normalized to the total CM fraction of the untreated DMD hiPSC-CMs. **(D)** Quantification of the NADPH-dependent superoxide production of NOX4 in the total CM fraction of DMD hiPSC-CMs upon 2.5 and 5.0 mM ATP addition, with or without idebenone treatment. Each data point was represented as percentage (%), normalized to the total CM fraction of the idebenone-treated DMD hiPSC-CM cultures. Data were representative of four or six independent experiments (n = 4 or n = 6) and values were expressed as mean ± SEM; *p < 0.05; **p < 0.01; ***p < 0.001 and ****p < 0.0001. Colored rectangles represented the independent experiments. Quantification of the NADPH-dependent superoxide production of NOX4 in the mitochondrial **(E)** and CM fraction **(F)** of hiPSC-CMs derived from DMD, DMD isogenic and healthy controls with or without idebenone treatment. **(G-H)** ATP luminescence detection showing the effect of idebenone treatment on the ATP levels in hiPSC-CMs cultures. Each data point was represented as percentage (%), normalized to the untreated DMD hiPSC-CM cultures. Data were representative of three independent experiments (n = 3) and values were expressed as mean ± SEM; *p < 0.05; **p < 0.01; ***p < 0.001 and ****p < 0.0001. Colored rectangles represented the independent experiments.

Table S1: Characteristics of DMD subjects and hiPSC lines.

	ID	DMD #2	DMD #5	DMD #6	DMD #2 isogenic	HC #1	HC #2	HC #3
	Origin	hFs	hPBMCs	hPBMCs	DMD #2	hPBMCs	hFs	hFs
	Mutation	pt.mut. exon 35 (c.4,996C > T; p.Arg1,666X)	del. exon 51-55	del. exon 46-51	CRISPR-Cas9 correction pt.mut. exon 35	NA	NA	NA
	Category	diseased	diseased	diseased	healthy	healthy	healthy	healthy
Phenotype	**Age start steroids**	7.5 years	4.5 years	6.5 years	NA	NA		
Phenotype	**Age loss of ambulation**	8.5 years	10 years	11 years				
Cardiomyopathy	**FS < 30%**	yes, 29%	no, 32%	no, 32%				
Cardiomyopathy	**EF**	50%	66%	61%				
Cardiomyopathy	**Measured at age**	20 years	9 years	20 years				
Cardiomyopathy	**Age at onset**	10 Years	NA	NA				
Pulmonary function	**FVC < 50%**	yes, 7%	no, 80%	yes, 19%				
Pulmonary function	**Measured at age**	25 years	9 years	19 years				

All DMD and control lines were previously characterized in-house or already published.
In the current study, somatic cells from DMD subjects were used to generate three diseased hiPSC lines DMD #2, DMD #5 and DMD #6 (Patel et al., 2019). Four different human control lines were used: (1) the DMD isogenic control line was in-house generated through CRISPR-Cas9 gene editing, as described in Materials and Methods; (2) HC #1 is commercially available from Thermo Fisher Scientific (Catalog number A18945); (3) HC #2 was kindly provided by Prof. C. Verfaillie (University of Leuven, Belgium) and generated by transduction of the new-born male fibroblast BJ1 cell line, as published by Coll et al. (Coll et al., 2018); and (4) HC #3 was a gift from Prof. P. Jennings (Medizinische Universität Innsbruck, Austria) to Prof. C. Verfaillie and generated by SeV-based reprogramming of male donor fibroblasts (SBAD2), as published by Rauch et al. (Rauch et al., 2018).
DMD: Duchenne muscular dystrophy; HC: healthy control; hPBMCs: human peripheral blood mononuclear cells; hFs: human fibroblasts; FS: fractional shortening; EF: ejection fraction; FVC: forced vital capacity; NA: not applicable.

Table S2: List of primers for Quantitative Real-Time PCR.

Gene	Primer direction	Primer sequence (5' > 3')
c-MYC	forward	TCCTCGGATTCTCTGCTCTCCT
	reverse	AGAAGGTGATCCAGACTCTGACCT
Dystrophin	forward	ATGCTTTGGTGGGAAGAAGT
	reverse	GGGCATGAACTCTTGTGGAT
GAPDH	forward	TCAAGAAGGTGGTGAAGCAGG
	reverse	ACCAGGAAATGAGCTTGACAAA
GDF-3	forward	ACACCTGTGCCAGACTAAGATGCT
	reverse	TGACGGTGGCAGAGGTTCTTACAA
HPRT	forward	TGACACTGGCAAAACAATGCA
	reverse	GGTCCTTTTCACCAGCAAGCT
hTERT	forward	AAATGCGGCCCCTGTTTCT
	reverse	CAGTGCGTCTTGAGGAGCA
KLF-4	forward	CGGACATCAACGACGTGAG
	reverse	GACGCCTTCAGCACGAACT
MALAT1	forward	GGACTTGCCTCAACTCCCTC
	reverse	GCCCTCTCAGCCACTCAAAT
MYH6	forward	GCCCTTTGACATTCGCACTG
	reverse	CGGGACAAAATCTTGGCTTTGA
MYH7	forward	ACTGCCGAGACCGAGTATG
	reverse	GCGATCCTTGAGGTTGTAGAGC
MYL2	forward	TTGGGCGAGTGAACGTGAAAA
	reverse	CCGAACGTAATCAGCCTTCAG
MYL7	forward	ACATCATCACCCACGGAGAAGAGA
	reverse	ATTGGAACATGGCCTCTGGATGGA
NANOG	forward	TGGCCGAAGAATAGCAATGGTGTG
	reverse	TTCCAGGTCTGGTTGCTCCACATT
NOX2	forward	TGCCAGTCTGTCGAAATCTGC
	reverse	ACTCGGGCATTCACACACC
NOX4	forward	TCCGGAGCAATAAGCCAGTC
	reverse	CCATTCGGATTTCCATGACAT
OCT4	forward	CGAGCAATTTGCCAAGCTCCTGAA
	reverse	GCCGCAGCTTACACATGTTCTTGA
p22^{phox}	forward	TACTATGTTCGGGCCGTCCT
	reverse	CACAGCCGCCAGTAGGTA
p47^{phox}	forward	GGGGCGATCAATCCAGAGAAC
	reverse	GTACTCGGTAAGTGTGCCCTG
p67^{phox}	forward	CCAGAAGCATTAACCGAGACAA
	reverse	CCTCGAAGCTGAATCAAGGC
RAC1	forward	ATGTCCGTGCAAAGTGGTATC
	reverse	CTCGGATCGCTTCGTCAAACA
RAC2	forward	TCTGCTTCTCCCTCGTCAG
	reverse	TCACCGAGTCAATCTCCTTGG
RAC3	forward	CTTCGAGAATGTTCGTGCCAA
	reverse	CCGCTCAATGGTGTCCTTG
REX1	forward	TGGAGGAATACCTGGCATTGACCT
	reverse	AGCGATTGCGCTCAGACTGTCATA
RPL13a	forward	CCTGGAGGAGAAGAGGAAAGAGA
	reverse	TTGAGGACCTCTGTGTATTTGTCAA
SOX2	forward	TGGCGAACCATCTCTGTGGT
	reverse	CCAACGGTGTCAACCTGCAT
TNNI1	forward	CCCAGCTCCACGAGGACTGAACA
	reverse	TTTGCGGGAGGCAGTGATCTTGG
TNNI3	forward	GATGCGGCTAGGGAACCTC
	reverse	GCATAAGCGCGGTAGTTGGA

Table S3: List of antibodies for flow cytometry (FC), immunostaining (IF) and western blot (WB).

Protein	Antibody name (#catalog number)	Provider	FC	IF	WB
ACTA2	Anti-Alpha Smooth Muscle Actin (Mouse monoclonal) **(#A2547)**	Merck		1:300	
ACTB	Beta Actin (13E5) (Rabbit monoclonal) **(#4970)**	Cell Signaling Technology			1:1,000
ACTN2	Anti-Sarcomeric Alpha Actinin (EA-53) (Mouse monoclonal) **(#ab9465)**	Abcam			1:100
AFP	Anti-Human Alpha-1-Fetoprotein (Rabbit polyclonal) **(#A0008)**	Dako		1:150	
Annexin V	APC Annexin V **(#550474)**	BD Pharmingen	1:20		
CASP3 (cleaved)	Cleaved Caspase-3 (Asp175) (Rabbit polyclonal) **(#9661)**	Cell Signaling Technology			1:500
CASP3 (full length)	Caspase-3 (Rabbit polyclonal) **(#9662)**	Cell Signaling Technology			1:1,000
cTnT	Recombinant Anti-Cardiac Troponin T (EPR3696) (Rabbit monoclonal) **(#ab92546)**	Abcam		1:100	
p22^{phox}	Anti-Cytochrome b245 Light Chain/p22-phox (44.1) (Mouse monoclonal) **(#ab80896)**	Abcam			1:100
Dystrophin (DMD)	DYS1 (Rod Domain) (Mouse monoclonal) **(#NCL-DYS1)**	Leica Novocastra		1:25	
Dystrophin (DMD)	DYS2 (C-terminus) (Mouse monoclonal) **(#NCL-DYS2)**	Leica Novocastra		1:25	
Dystrophin (DMD)	DYS3 (N-terminus) (Mouse monoclonal) **(#NCL-DYS3)**	Leica Novocastra		1:25	
LIN28	LIN-28 (S-15) (Goat polyclonal) **(#sc-54032)**	Santa Cruz Biotechnology		1:50	
NANOG	Nanog (Rabbit polyclonal) **(#PA1-097)**	Thermo Fisher Scientific		1:200	
NOX4	Anti-NADPH Oxidase 4 (Rabbit monoclonal) **(#ab133303)**	Abcam	1:2,175		1:1,000
OCT4	Anti-Oct4 - Embryonic Stem Cell Marker (Goat polyclonal) **(#ab27985)**	Abcam		1:200	
PARP	PARP (46D11) (Rabbit monoclonal) **(#9532)**	Cell Signaling Technology			1:1,000
SIRPA	PE Anti-Human CD172a/b (SIRPα/β) **(#323806)**	BioLegend	1:100		
SOX2	Sox-2 (Y-17) (Goat polyclonal) **(#sc-17320)**	Santa Cruz Biotechnology		1:50	
SSEA4	SSEA-4 (MC813) (Mouse monoclonal) **(#sc-59368)**	Santa Cruz Biotechnology		1:50	
TRA-1-60	TRA-1-60 (TRA-1-60) (Mouse monoclonal) **(#sc-21705)**	Santa Cruz Biotechnology		1:50	
TUBB	Beta Tubulin (Rabbit monoclonal) **(#NB110-57610)**	NovusBio		1:250	

SUPPLEMENTAL EXPERIMENTAL PROCEDURES

Study design and ethics statement

The objective of this study is to develop a stem cell-based model to investigate pathological mechanisms and evaluate their therapeutical potential in cardiomyopathy in DMD patients. The study was conducted in compliance with the principles of the Declaration of Helsinki, the principles of 'Good Clinical Practice' (GCP) and in accordance with all applicable regulatory requirements. The use of human samples from healthy control donors and DMD subjects for experimental purposes and protocols in the present study was approved by the Ethics Committee of the University Hospitals Leuven (respectively, S55438 and S65190). Subjects information, used in this study, is summarized in Table S1.

Chemicals and reagents

NAC (Merck), ataluren (PTC124; Selleckchem) and idebenone (Santhera Pharmaceuticals, Pratteln Switzerland). STS (Merck). CM-H_2DCFDA Total Intracellular ROS Indicator, JC-1 Mitochondrial Membrane Potential Probe, MitoSOX Red Mitochondrial Superoxide Indicator and MitoTracker-Red CMXRos Mitochondria Probe (all from Thermo Fisher Scientific). ATP Solution, Luminescent ATP Detection Assay Kit, Colorimetric NADPH Assay Kit (both from Abcam) and Mitochondrial Isolation Kit for Cultured Cells (Thermo Fisher Scientific).

Generation of integration-free DMD hiPSCs

hFs and hPBMCs were isolated from DMD patients with known *Dystrophin* mutations (Table S1). Somatic cells were reprogrammed towards pluripotency using the integration-free SeV-based technology, performed according to the manufacturer's instructions (CytoTune-iPS 2.0 Sendai Reprogramming Kit; Thermo Fisher Scientific).

Teratoma formation assay

Pluripotency of SeV-reprogrammed hiPSCs was evaluated *in vivo* in 6- to 8-week-old immunodeficient *Rag2-null γc-null*/Balb/C mice. Teratoma formation experiments in mice were conducted following the guidelines of the Animal Welfare Committee of Leuven University and Belgian/European legislation (approved July 2016; P174/2016).

Generation of DMD isogenic control line through CRISPR-Cas9 genome editing

To restore full-length expression of the *Dystrophin* gene, the isogenic control for the DMD hiPSC patient line, characterized by a genetic point mutation in exon 35 (c.4,996C > T; p.Arg1,666X) of the *Dystrophin* gene, was generated through CRISPR-Cas9 from the *S. pyogenes* system (5'-NGG PAM) as previously described (Ran et al., 2013). Briefly, two 20-nucleotide sgRNAs (sgRNA #1: FW seq. CACCG-ATTTAACCACTCTTCTGCTC and RV seq. AAAC-GAGCAGAAGAGTGGTTAAAT-C; sgRNA #2: FW seq. CACCG-TAACCACTCTTCTGCTCAGG and RV seq. AAAC-CCTGAGCAGAAGAGTGGTTA-C) were designed and ligated into the RNA-guided nuclease plasmid (pX330-mCherry plasmid; Addgene), in order to induce the Cas9-mediated DSB in the genomic DNA of the Dystrophin-deficient hiPSCs. Cas9-mediated genome editing was performed via HDR. The targeted DNA modification required the use of a plasmid-based donor repair template with two homology arm regions for the *Dystrophin* gene, flanking a GFP-Hygromycin-TK expressing cassette for selection. Here, one of the homology arms contained the genetic correction of the nonsense mutation in the *Dystrophin* gene. Finally, a completely gene editing-free DMD isogenic hiPSC line was obtained due to PiggyBac excision and Fialuridine (FIAU; Merck) selection, restoring the expression of functional Dystrophin protein (Table S1).

Quantitative Real-Time PCR analysis

Total RNA was extracted using the PureLink RNA Mini Kit and treated with the TURBO DNA-Free DNase Kit to assure highly pure RNA. 1 μg RNA was reverse transcribed into cDNA with SuperScript III Reverse Transcriptase First-Strand Synthesis SuperMix. Quantitative Real-Time PCR was performed with the Platinum SYBR Green qPCR SuperMix-UDG (all from Thermo Fisher Scientific). The oligonucleotide primer sequences (all from IDT) are listed in Table S2. A 10-fold dilution series ranging from 10^{-3} to 10^{-8} of 50 ng/μL human genomic DNA was used to evaluate the primer efficiency. Delta Ct (ΔCt) values were calculated by subtracting the Ct values from the genes of interest with the Ct values of the housekeeping genes (*GAPDH, HPRT* and *RPL13a*).

Flow cytometric analysis

Differentiated hiPSC-CMs were dissociated using Collagenase A (1 U/mL) for 20 minutes at 37°C. All flow cytometry procedures were performed according to the manufacturer's instructions. Hank's

Balanced Salt Solution (HBSS; pH 7.2) with $CaCl_2$ and $MgCl_2$ supplemented with 2% FBS (both from Thermo Fisher Scientific), 10 mM HEPES and 10 mM NaN_3 (both from Merck), was used as staining buffer. For high CM purity, hiPSC-CMs were stained for the surface marker SIRPA (data not shown). If intracellular staining was necessary, cells were fixed with 4% paraformaldehyde (PFA; Polysciences) for 10 minutes at 37°C and permeabilized in ice-cold 90% methanol (Merck) for 30 minutes on ice, before the staining procedure. Fluorescence minus one (FMO) controls and compensations were included for appropriate gating. Samples were analyzed using the FACS Canto II HTS (BD Biosciences) and quantified using FlowJo Software Version 10 (FlowJo LLC). Table S3 provides a list of all flow cytometric antibodies used in this study.

Immunofluorescence imaging

Cells were fixed with 4% PFA for 10 minutes at 4°C, permeabilized for 30 minutes at room temperature in PBS supplemented with 0.2% Triton X-100 and 1% Bovine Serum Albumin (BSA) and blocked for 30 minutes at room temperature in 10% donkey serum (all from Merck). Samples were stained overnight at 4°C with the primary antibodies, followed by the appropriate secondary antibodies (1 h incubation at room temperature). Immunofluorescent primary and secondary antibodies were listed in Table S3. Nuclei were counterstained with 10 μg/mL Hoechst (33342; Thermo Fisher Scientific). Analyses were assessed using the Nikon Eclipse Ti Microscope or the Nikon Eclipse Ti A1R Configurated Confocal Microscope, with appropriate NIS-Elements Software (all from Nikon).

Mitochondria and cytoplasmic fractionation

Mitochondrial and cytoplasmic separation was performed using the Mitochondrial Isolation Kit for Cultured Cells (Thermo Fisher Scientific), according to the manufacturer's instructions with minor modifications. To obtain a more purified mitochondrial fraction (with a more than 50% reduction of the lysosomal and peroxisomal contaminants), the post-cell debris supernatant was subjected to an extra centrifuge step at 3000 x g for 15 minutes. For Western blot analysis, mitochondrial pellets were lysed with 2% CHAPS (Merck) in Tris-buffered saline (TBS; containing 25 mM Tris, 0.15 M NaCl; pH 7.2) and subsequently centrifuged at high speed for 2 minutes. Western blot analysis was performed on the supernatant, containing soluble mitochondrial protein.

Western blot analysis

Western blot analysis for cell lysates was performed in RIPA buffer supplemented with 10 mM NaF, 0.5 mM Na_3VO_4, 1:100 protease inhibitor cocktail and 1 mM Phenylmethylsulfonyl Fluoride (PMSF; all from Merck). Equal amounts of protein (40 μg) were heat-denaturated at 95°C in sample-loading buffer (50 mM Tris-HCl, 100 mM DTT, 2% SDS, 0.1% bromophenol blue and 10% glycerol; pH 6.8), resolved by SDS-polyacrylamide gel electrophoresis and subsequently transferred to nitrocellulose membranes (Amersham Protran Western Blotting Membranes; Merck). The filters were blocked with TBS containing 0.05% Tween and 5% non-fat dry milk (Merck). Incubation was done overnight with the indicated primary antibody dilutions, as listed in Table S2. Horseradish peroxidase-conjugated secondary antibodies (Bio-Rad) were diluted 1:5,000 in TBS-Tween (0.05%) with 2.5% non-fat dry milk. After incubation with SuperSignal Pico or Femto chemiluminescence substrate (both from Thermo Fisher Scientific), the polypeptide bands were detected with GelDoc Chemiluminescence Detection System (Bio-Rad). Quantification of relative densitometry was obtained by normalizing to the background and to loading control proteins (ACTB, from Cell Signaling Technology) using Image Lab Software (Bio-Rad).

Patch-clamp electrophysiology and Ca^{2+} recordings

Single cells were seeded on Matrigel-coated coverslips. Cells were perfused at 37°C with a solution containing the following (in mM): 137 NaCl, 5.4 KCl, 1.8 $CaCl_2$, 0.5 $MgCl_2$, 10 glucose and 10 Na-HEPES. The pH was adjusted to 7.4 with NaOH. The patch-clamp pipettes were filled with a solution containing the following (in mM): 120 K-Asp, 20 KCl, 10 HEPES, 5 Mg-ATP, 10 NaCl and 0.05 K_5Fluo-4. The pH was adjusted to 7.2 with KOH. Patch electrode resistances were between 2.5 and 3 MΩ when the pipettes were filled with intracellular solution. Cells were patched in the whole-cell configuration. Data were recorded using an Axopatch 200B amplifier (Axon Instruments) at a sampling rate of 10 kHz. Signals were filtered with 5 kHz low-pass Bessel filters. APs were recorded in current-clamp mode, and if not spontaneous, after a 5 ms pulse of 0.5 nA at a 1 Hz frequency. Ca^{2+} currents were measured in voltage-clamp mode. After a Na^+ current inactivation step from -70 mV to 40 mV for 750 ms, Ca^{2+} currents were recorded with 10 mV voltage steps from -40 mV to 60 mV during 205 ms. For analysis, the maximum amplitude of the Ca^{2+} current was measured and corrected for the cell capacitance. Data were analyzed with Clampfit Software (Axon Instruments).

Contractility measurements of 3D EHT constructs

The contractile properties of 3D EHTs were monitored by measuring the deflection distances of the microposts of the EHT device (in μm) during spontaneous contraction and relaxation under temperature-controlled conditions (37°C) in oxygenated Tyrode's solution (in mM; containing 137 NaCl, 5.4 KCl, 0.5 $MgCl_2$, 12.8 HEPES and 5.5 Glucose; dissolved in deionized sterile water at pH 7.4) with Ca^{2+}. A Ca^{2+} concentration of 1.8 mM was used to mimic physiological conditions. EHT constructs for contractility measurements were generated from 8-day-old hiPSC-CMs and monitored after 5 days of EHT maturation.

ATP luminescence detection

The levels of cellular ATP were measured using the Luminescent ATP Detection Assay Kit (Abcam), according to the manufacturer's instructions. The Luminescent ATP Detection Assay Kit is based on the production of light caused by the reaction of ATP with added firefly's luciferase and luciferin. The ATP concentration is proportional to the emitted light. Briefly, hiPSC-CMs (20,000 cells per well in 100 μL volume) were seeded in a 96-well white microplate. Next day, 50 μL of cell lysis solution was added to each well and the plate rotated for 5 minutes using an orbital shaker at 700 rpm to lyse cells and stabilize ATP. The plate was kept in the dark for 10 minutes and recordings were performed with the EG&G Berthold Microplate Luminometer LB 96V and corresponding software (Berthold Technologies) (Shanmugasundaram et al., 2017).

Measurements of NADPH-dependent ROS production

The Colorimetric NADPH Assay Kit (Abcam) provides a convenient method for detecting NADPH in contrast to the traditional NAD/NADH and NADP/NADPH assays (which monitor the changes in NADH or NADPH absorption at 340 nm, suffering low sensitivity and high interference) (Griendling et al., 2016). Here, the NADPH probe is a chromogenic sensor that has its maximum absorbance at 460 nm upon NADPH reduction. The absorption of the NADPH probe is directly proportional to the concentration of NADPH. NADPH-dependent ROS production was measured in the presence or absence of 2.5 or 5.0 mM ATP (preincubated for 60 minutes) in the total CM fraction or isolated mitochondrial fraction, according to the manufacturer's instructions. Briefly, hiPSC-CMs (20,000 cells per well in 100 μL volume) were seeded in a 96-well black microplate with clear flat bottoms. NADPH probe was added to samples and incubated for 30 minutes and protected from light. Recordings were performed with the ELx808 Absorbance Microplate Reader with absorbance measurements at 460 nm and quantified using Gen5 Software Version 3 (both from BioTek Instruments) (Sambon et al., 2020).

Statistical analysis

Data were statistically analyzed using Prism Software Version 8 (GraphPad). All data were reported as mean ± standard error of the mean (SEM). Differences between two groups were examined for statistical significance using Student's t-test. One-Way or Two-Way ANOVA (with multiple comparisons test and Tukey's or Bonferroni's correction) were used for three or more groups. Significance of the difference was indicated as follows: *$p < 0.05$; **$p < 0.01$; ***$p < 0.001$ and ****$p < 0.0001$.

SUPPLEMENTAL REFERENCES

Coll, M., Perea, L., Boon, R., Leite, S.B., Vallverdu, J., Mannaerts, I., Smout, A., El Taghdouini, A., Blaya, D., Rodrigo-Torres, D., et al. (2018). Generation of Hepatic Stellate Cells from Human Pluripotent Stem Cells Enables In Vitro Modeling of Liver Fibrosis. Cell Stem Cell *23*, 101-113 e107. 10.1016/j.stem.2018.05.027.

Griendling, K.K., Touyz, R.M., Zweier, J.L., Dikalov, S., Chilian, W., Chen, Y.R., Harrison, D.G., Bhatnagar, A., and American Heart Association Council on Basic Cardiovascular, S. (2016). Measurement of Reactive Oxygen Species, Reactive Nitrogen Species, and Redox-Dependent Signaling in the Cardiovascular System: A Scientific Statement From the American Heart Association. Circ Res *119*, e39-75. 10.1161/RES.0000000000000110.

Patel, A.M., Wierda, K., Thorrez, L., van Putten, M., De Smedt, J., Ribeiro, L., Tricot, T., Gajjar, M., Duelen, R., Van Damme, P., et al. (2019). Dystrophin deficiency leads to dysfunctional glutamate clearance in iPSC derived astrocytes. Transl Psychiatry *9*, 200. 10.1038/s41398-019-0535-1.

Ran, F.A., Hsu, P.D., Wright, J., Agarwala, V., Scott, D.A., and Zhang, F. (2013). Genome engineering using the CRISPR-Cas9 system. Nat Protoc *8*, 2281-2308. 10.1038/nprot.2013.143.

Rauch, C., Feifel, E., Kern, G., Murphy, C., Meier, F., Parson, W., Beilmann, M., Jennings, P., Gstraunthaler, G., and Wilmes, A. (2018). Differentiation of human iPSCs into functional podocytes. PLoS One *13*, e0203869. 10.1371/journal.pone.0203869.

Sambon, M., Gorlova, A., Demelenne, A., Alhama-Riba, J., Coumans, B., Lakaye, B., Wins, P., Fillet, M., Anthony, D.C., Strekalova, T., and Bettendorff, L. (2020). Dibenzoylthiamine Has Powerful Antioxidant and Anti-Inflammatory Properties in Cultured Cells and in Mouse Models of Stress and Neurodegeneration. Biomedicines *8*. 10.3390/biomedicines8090361.

Shanmugasundaram, K., Nayak, B.K., Friedrichs, W.E., Kaushik, D., Rodriguez, R., and Block, K. (2017). NOX4 functions as a mitochondrial energetic sensor coupling cancer metabolic reprogramming to drug resistance. Nat Commun *8*, 997. 10.1038/s41467-017-01106-1.